AWARD NUMBER: W81XWH-13-1-0073

TITLE: 7T Magnetization Transfer and Chemical Exchange Saturation Transfer MRI of Cortical Gray Matter: Can We Detect Neurochemical and Macromolecular Abnormalities?

PRINCIPAL INVESTIGATOR: Seth A. Smith

CONTRACTING ORGANIZATION: Vanderbilt University

REPORT DATE: October 2014

TYPE OF REPORT: Annual

PREPARED FOR: U.S. Army Medical Research and Materiel Command
Fort Detrick, Maryland 21702-5012

REPORT DOCUMENTATION PAGE

Form Approved
OMB No. 0704-0188

1. REPORT DATE	2. REPORT TYPE	3. DATES COVERED
10/21/2014	Annual	30 Sep 2013 – 29 Sep 2014

4. TITLE AND SUBTITLE
7T Magnetization Transfer and Chemical Exchange Saturation Transfer MRI of Cortical Gray Matter: Can We Detect Neuro-chemical and Macromolecular Abnormalities?

5a. CONTRACT NUMBER

5b. GRANT NUMBER - W81XWH-13-1-0073

5c. PROGRAM ELEMENT NUMBER

6. AUTHOR(S)
Seth Smith

E-Mail: seth.smith@vanderbilt.edu

5d. PROJECT NUMBER

5e. TASK NUMBER

5f. WORK UNIT NUMBER

7. PERFORMING ORGANIZATION NAME(S) AND ADDRESS(ES)

The Vanderbilt University
Nashville, TN 37240-0001

8. PERFORMING ORGANIZATION REPORT NUMBER

9. SPONSORING / MONITORING AGENCY NAME(S) AND ADDRESS(ES)

U.S. Army Medical Research and Materiel Command
Fort Detrick, Maryland 21702-5012

10. SPONSOR/MONITOR'S ACRONYM(S)

11. SPONSOR/MONITOR'S REPORT NUMBER(S)

12. DISTRIBUTION / AVAILABILITY STATEMENT

Approved for Public Release; Distribution Unlimited

13. SUPPLEMENTARY NOTES

14. ABSTRACT
We present the first annual report for this project. We have developed and deployed a quantitative MRI set of MRI scans at 7T in healthy volunteers and have developed an analysis pipeline for the quantification of macromolecular and metabolic indices reflective of demyelination and neurotransmitter/protein accumulation. All quantitative MRI methods deployed in humans were optimized and vetted via phantom work and simulation. We are happy to report initial findings that show excellent image quality and differences between the normal cohort and one MS patient. Additionally, we have developed, in conjunction with Dr. Newhouse, a neurocognition expert, an extensive neuropsychiatric battery for correlation studies in year 2. We have had excellent recruitment and retention and look forward to group comparisions in year 2.

15. SUBJECT TERMS -Not Provided

16. SECURITY CLASSIFICATION OF:			17. LIMITATION OF ABSTRACT	18. NUMBER OF PAGES	19a. NAME OF RESPONSIBLE PERSON
a. REPORT	b. ABSTRACT	c. THIS PAGE			USAMRMC
U	U	U	UU		19b. TELEPHONE NUMBER *(include area code)*

Table of Contents

INTRODUCTION:
We recognize that many patients with Multiple Sclerosis (MS) suffer from cognitive impairment at some point in their disease course. However, characterization cognitive change in patients with MS has been difficult to pinpoint, and is hampered by poor quantitative markers. We have two hypotheses: 1) conventional imaging is insensitive to gray matter (GM) changes known to exist in patients with MS, and 2) ultra-high MRI field strengths (7T) would allow an opportunity to study the myelination and metabolic changes of the cortical GM in patients with MS and known cognitive impairment. The purpose of this proposal is to develop and implement a targeted quantitative magnetization transfer (qMT) and chemical exchange saturation transfer (CEST) MRI imaging paradigm at 7T to detect and quantify the level of myelin loss (qMT), protein/peptide changes (amide proton transfer CEST), neurotransmitter deficiencies (GluCEST) in the GM of patients with MS, and to relate these findings to neuropsychiatric evaluation outside the MRI scanner. The scope is to: 1) develop novel, high-resolution, high field, quantitative MRI methods sensitive to myelination and neurochemicals for implementation in the cortical GM of human populations, 2) deploy these methods in patients with MS, 3) relate these findings to measures of cognitive impairment, and 4) develop a lower MRI field strength alternative for direct patient impact.

KEYWORDS:
- Magnetic Resonance Imaging (MRI)
- 7 Tesla (7T)
- Chemical Exchange Saturation Transfer (CEST)
- Magnetization Transfer (MT)
- Brain
- Cortical Gray Matter (cGM)
- Multiple Sclerosis (MS)
- Functional MRI (fMRI)
- Pool Size Ratio (PSR)
- Amide Proton Transfer (APT)
- Glutamate (Glu)
- Myoinositol (mI)
- Cognitive Impairment

OVERALL PROJECT SUMMARY

Task 1. *IRB Preparation and Human Subjects Approvals.*
Completed

Task 2*. Develop, optimize and implement advanced, quantitative Magnetization Transfer (MT) and Chemical Exchange Saturation Transfer (CEST) in phantoms and evaluate minimum achievable resolution and the associated reliability of derived indices*

Simulation/Phantom Studies
The objective of this task was to develop a best-practice MT and CEST acquisition scheme to be deployed in Task 3 in healthy controls.

Summary of Results/Progress and Accomplishments

CEST –
APT-CEST – We have optimized through simulation and phantom studies a single-power, whole brain APT CEST acquisition for deployment in healthy volunteers and patients (Y2Q1). We began with the protocol presented by Jones et al (1) for whole brain coverage at 7T and increased the in-plane resolution, the coverage,

and modified the saturation scheme, readout, and fat-saturation (now a binomial excitation pulse) to minimize distortions in the phantoms while maintaining sufficient contrast to noise (CNR) for the APT CEST signatures in a reasonable scan time (9 minutes). The relevant scan parameters are as follows:

- Whole Brain (33 slices) 3D Gradient Echo (FFE) with multi-shot EPI (factor = 7) readout
- 1.5 x 1.5 x 5mm^3 acquired resolution
- CEST RF Saturation B1 = 2μT x 25ms (each)
- 64 offset frequencies (Dw = -5 – 5ppm, Δω step = 0.2ppm + 14 no Saturation Scans)
- Total Scan Time = 9:10

The simulations were performed using a 3 pool model of the CEST effect presented by Zaiss et al (2) and inputting estimates for T1, T2, pool sizes and exchange rates for the macromolecular, labile (amide protons) protons, and water as follows: Simulations were designed to identify optimal CEST preparation (RF irradiation power and bandwidth) parameters for APT contrast. All simulations were carried out utilizing the scripting environment in MATLAB 2012b (Mathworks, Natick, Massachusetts) on an Apple iMac (Cupertino, CA; 3.0 GHz, dual core CPU). Theoretical saturation was modeled according to the Bloch equations for three pools: bulk water (free), semisolid macromolecular (conventional MT), and mobile macromolecular (CEST) pools. This was achieved using the simple matrix solution to numerically solve the Bloch equations (3). This model assumes a T2-dependent Super-Lorentzian absorption lineshape for the macromolecules (4). Physical values of exchange rate, T1, and T2, were fixed according to (5,6). The bulk water was modeled as a Lorentizan with T1/T2 = 1538 ms/45ms. The semisolid macromolecular pool was modeled with T1/T2/exchange rate = 1600ms/0.01ms/20 Hz with offset = -2.34ppm (7). The labile proton pool was modeled as a Lorentzian with T1/T2/exchange rate = 500ms/20ms/50Hz with offset = 3.5ppm and a concentration of 0.001 compared to bulk water (1.0) and macromolecular pool (0.1). Therefore our simulations included a single RF irradiation, a brief delay for spoiling, an on-resonance excitation, and a delay for readout. The B_1 amplitude (power) was varied over amplitudes from 1 μT to 3 μT while holding the duration constant at 25 ms. The B_1 amplitude was subsequently fixed to 1 μT while the pulse duration was varied from 0 ms to 60 ms.

For phantom scans, we performed the above paradigm at various in-plane resolutions as low as 0.75mm^2, but determined through curve analysis that at these resolutions the CNR was insufficient to parse out the CEST effect from the background noise. From these simulations and phantom studies, the above pulse sequence paradigm was chosen to maximize CEST contrast derived from APT.

GluCEST – For glutamate, we performed the same simulations as above, but we modeled the off-resonance saturation as given in (8), and assumed an exchange rate for glutamate = 100 Hz, pool size = 0.001 compared to bulk water (1.0) and macromolecular concentration (0.01) and Δω = 3.0ppm. For the GluCEST acquisition, due the concern of overlapping resonances (GABA, Glutamate, and other Amines) a high-spectral resolution acquisition needed to be obtained (Δω = 0.2ppm spacing), thus scan time becomes prohibitive for extremely high resolution. However, it should be pointed out that the amine resonances that may reside in juxtacortical WM will be significantly less than the adjacent GM, so a slightly poorer resolution acquisition will not be problematic if a high spectral resolution scan is obtained. We therefore, decided to utilize a scan very similar to that which as been presented by Dr. Reddy (8,9) and thus we will implement a single slice GluCEST acquisition in vivo at a resolution of 1.9 x 1.9 x 5mm^3.

- Single Slice (2D) Gradient Echo (FFE) with multi-shot TFE (40 shots) readout
- 1.9 x 1.9 x 5mm^3 acquired resolution
- CEST RF Saturation B1 = 4.25μT x 10ms (each) x 100segments at 90% duty cycle
- 50 offset frequencies (Δω = -5 – 5ppm, Δω step = 0.2ppm)
- Total Scan Time = 11:36

qMT –

We have chosen to implement the selective inversion recovery (SIR) quantitative MT (qMT) to quantitatively extract the pool size ratio (PSR), which has been shown to be reflective of myelin. We have developed the SIR

approach at 7T as discussed in the Q1Y1 and Q2Y1 progress reports. This pulse sequence has been shown in previous reports, published (10) and provided in Appendix 3. However, in Q3Y1, we studied via simulation the impact of partial volume effects where we know there is a non-negligible MT effect in GM and certainly a strong effect in WM. Thus, in juxtacortical voxels where a blend of GM and WM may occur, poorer in-plane resolution results in an inability for the model to remain stable when deriving the PSR values (i.e. two different PSR values may fit equally well when there are two populations within a voxel). Therefore, we proposed a reduced number of slices but increased the in-plane resolution. From simulations, we feel that this provides the most robust acquisition method to be deployed in patients. Thus, from our phantom studies, we have determined that a 1 x 1 x 2mm^3 acquisition with 5 slices sampled at 14 TIs (TI = 6ms, 10ms, 16ms, 26ms, 42ms, 68ms, 110ms, 178ms, 288ms, 468ms, 760ms, 1233ms, 2000ms, 8000ms) will be performed in patients with MS and healthy controls.

- Inversion prepared 3D Gradient Echo (FFE) with multi-shot TFE (2 shots) readout
- 1 x 1 x 2mm3 acquired resolution (5 slices)
- 14 Inversion Times (TI = 6ms, 10ms, 16ms, 26ms, 42ms, 68ms, 110ms, 178ms, 288ms, 468ms, 760ms, 1233ms, 2000ms, 8000ms) at a constant delay time (TD = 2500ms)
- Total Scan Time = 10:11

Conclusion of Task 2: Simulation and Phantom-optimized qMT and CEST acquisitions

Through simulation and phantom studies, we have devised a final protocol to be deployed in healthy volunteers and patients with MS. A summary of the protocol is given below, and a complete protocol is given in Appendix 1.

Final Summary of Protocol implemented in healthy controls (Task 3) and patients with MS (Task 5).

- Constant RF APT CEST – 9:10
- Constant RF GluCEST – 11:36
- SIR qMT – 10:11
- Bloch-Siegert B1 mapping – 1:42
- Dual-echo B0 mapping – :04
- T1w MPRAGE Anatomical – 2:12
- fMRI Resting State – 8:34
- fMRI N-Back task – 8:30
- fMRI Trailmaking task – 4:14

The current scan time for all scans is approximately 1 hour.

Task 3 – Implement current best practice for MT and CEST in healthy volunteers and evaluate reliability

The objective of this task was to implement a best-practice MT and CEST acquisition scheme in healthy controls.

Summary of Results/Progress and Accomplishments

The above protocol has been implemented in 20 healthy volunteers at the close of year 1. We have additionally repeated this paradigm in 8 healthy volunteers. We have further scheduled the remainder of the healthy controls to be scanned in the coming month. There is one delay to report in that at the close of Year 1, our SOW stated that we would have recruited 50 healthy volunteers into the study. As pointed out in quarterly reports Q1Y1 and Q2Y1, we struggled initially making the phantoms to study the impact of resolution on the final protocol. This resulted in less than the expected 50 healthy controls. However, we have already scheduled these remainder healthy volunteers, and have a 40% return rate on for repeat visits to understand the reproducibility. We will complete the healthy volunteers and repeat visits in Q1Y1

In a follow-up to the Q3Y1 report, we have added three fMRI scans in collaboration with Dr. Paul Newhouse, our neurocognition expert. It is important that we note that this does not change the scope, but rather offers a unique opportunity to study the cognitive function in the MRI in healthy volunteers and patients for greater understanding of the relationship between the advanced, quantitative measures and outside-scanner neurocognitive battery. This is exceptionally unique as neither of these three fMRI scans have been studied in MS patients with known cognitive impairment and creates an exceptionally rich data set to mine for understanding neurocognitive decline in MS patients.

In 20 healthy volunteers (with 8 repeat acquisitions), we have obtained the entire proposed MRI protocol as given above. Preliminary results follow under Task 4.

Task 4 – Analyze the derived indices in healthy volunteers and evaluate reproducibility (1 month)
The objective of this task was to 1) develop an analysis pipeline for constructing maps and deriving indices reflective of GM and juxtacortical WM from the quantitative MRI acquisitions prepared in Task 3, and 2) to ascertain these indices in preparation for analysis of reproducibility.

Summary of Results/Progress and Accomplishments

Develop an analysis pipeline for routine analysis of data generated.
As the first part of Task 4, we well understood the need to 1) correct patient motion in an individual scan (motion-correction), 2) co-register data across scans into the same space for robust analysis (co-registration), and 3) segmentation of WM and GM for histogram and descriptive statistics of each derived index.

WM/GM segmentation was performed in FAST using 3 classes as implemented in the FSL toolbox (FMRIB, Oxford, UK). The co-registration was performed using FNIRT (non-linear registration, FSL, FMRIB, Oxford, UK) to put the quantitative maps into the MPRAGE space such that the segmentation can be applied. To that end, Figure 1, shows two slices of an APT-CEST acquisition motion corrected and co-registered. The magenta color indicates the WM, and the green indicates the GM derived from the MPRAGE anatomical acquisition and overlaid on the APT map. It can clearly be seen that the agreement between the MPRAGE and the APT maps is high and the WM and GM clearly seen. The bottom panels show the process of joining the MPRAGE, the WM/GM Segmentation and the GluCEST-weighted acquisition for completeness.

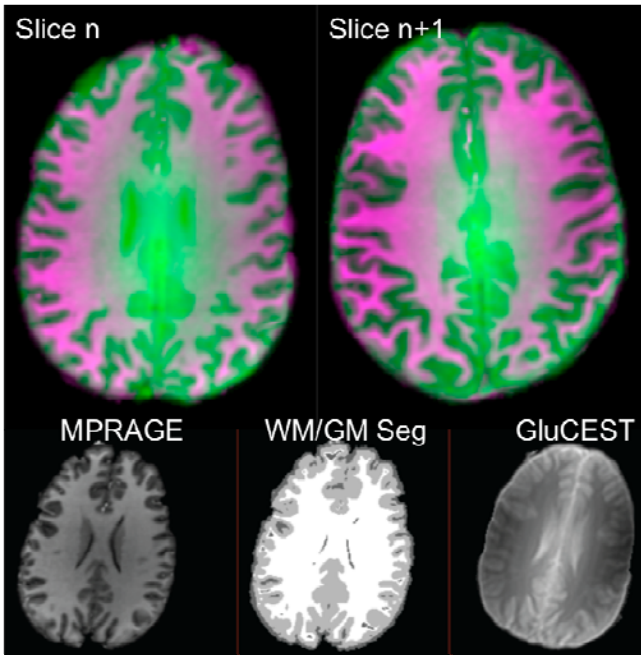

Figure 1 – (Top) coregistration and segmentation results applied to APT maps, and (bottom) the target (MPRAGE), segmented map, and GluCEST-weighted acquisition.

APT CEST analysis and results
We have constructed the APT CEST maps in the following manner. First, the CEST spectrum for each voxel is normalized, corrected for B1 drift and fit to a single-lorentizian (11) and the minimum spectral intensity is shifted to an offset ($\Delta\omega$) = 0 for B0 correction. After this correction, the difference between the data and the fit create a Lorentzian residual. The residual between $\Delta\omega$ = 3.25 and 3.75 are integrated and termed the APT Lorentzian. An example of this is shown in Figure 2A left panel. To assess reproducibility we created a single

CEST spectrum for the whole brain and compared visit 1 to visit 2. Figure 2A right panel shows the results of two healthy repeated studies, where the green/blue curves are subject 1, and magenta/black curves are subject two over two times points. As it can be seen, the reproducibility is high over the whole brain. Individual structure assessments are ongoing. It can also be appreciated the spectral quality of the CEST spectrum using this analysis approach.

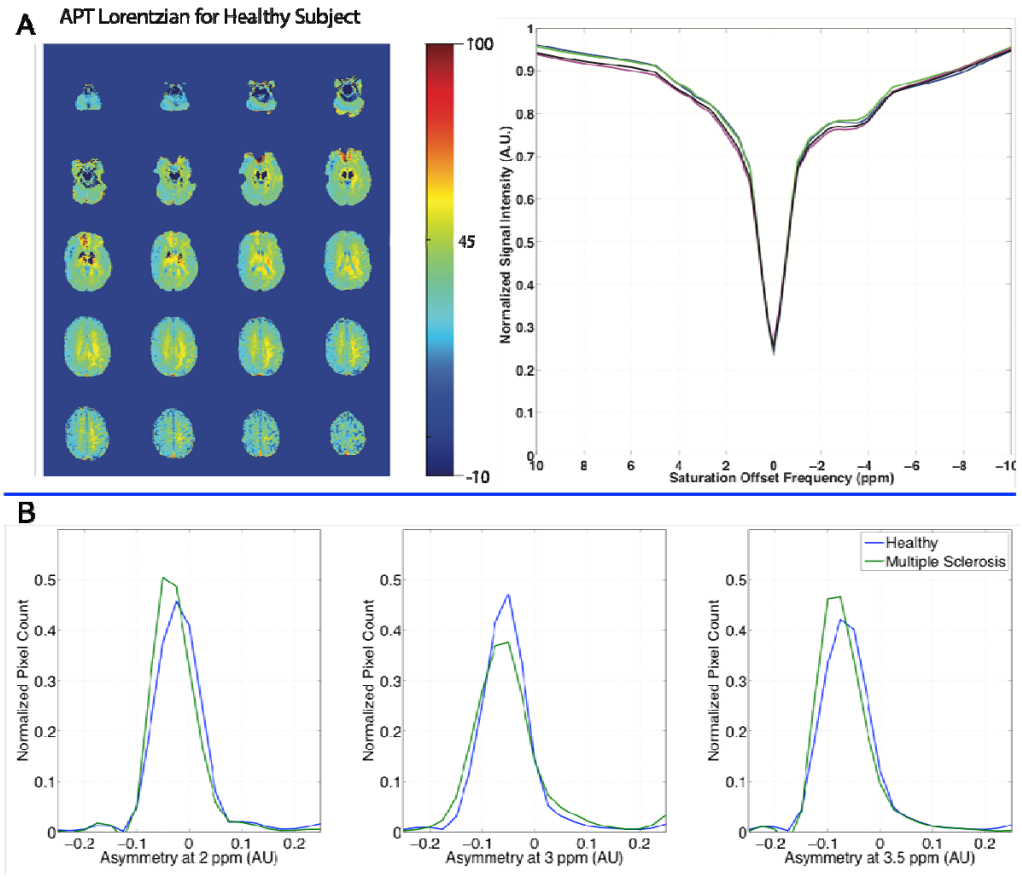

Figure 2: (A) APT maps for all slices derived in a healthy volunteer and concomitant test-retest CEST spectra in 2 healthy volunteers. The test-retest is over the whole brain, and the green/blue and magenta/black spectra pairs are from the same volunteers. (B) histogram analysis of segmented GM in 20 healthy volunteers and 1 MS patient with clinically noted cognitive impairment. Note that histograms at 2ppm and 3.5ppm show a downward shift of the MS patient relative to the healthy control indicating initial sensitivity to the pathology of cortical GM damage.

Once the data were segmented, we compared the GM averaged over all healthy volunteers (n = 20) and 1 MS patient with clinically diagnosed cognitive impairment via histogram analysis shown in Figure 2B. We performed the same calculation, but also examined resonances at 2ppm (hydroxyl and sensitive to myoinositol) and 3ppm (amine protons sensitive to GABA and Glutamate) and 3.5ppm (amide proton transfer – sensitive to pH and protein concentration). It should be pointed out that the 1 MS patient examined here is actually part of Task 5, but it is important to show here as it points towards the sensitivity of the measurement. In this one patient, there is an obvious downward shift of the GM histograms at 2ppm and 3.5ppm giving the impression that we are detecting cortical and perhaps even some sub-cortical changes in protein concentration and myoinositol. In Figure 2B, the green is the MS patient, and the blue is the average over healthy volunteers. We are exceptionally excited by this initial result and felt it important to share here as Task 5 will indeed prove the sensitivity of these advanced techniques to MS.

Glutamate CEST (GluCEST) analysis and results

GluCEST analysis proceeded as presented in (8,9). We performed GluCEST analysis in 20 healthy volunteers and 4 MS patients at the time of this report, though only one had been analyzed and is presented here. In short, GluCEST-weighted images were collected for a single slice with high spectral saturation fidelity (see Task 2) at a slice slightly superior to the corpus callosum. Sample GluCEST weighted images are shown as a function of offset frequency in Figure 3, top panel. From these maps, the GluCEST spectra were corrected for B0 and B1 in the fashion presented in (9), and a GluCEST asymmetry map at $\Delta\omega$ = 3.0ppm was generated. Figure 3, bottom panel shows two healthy volunteers and one patient with MS, clinically diagnosed with cognitive

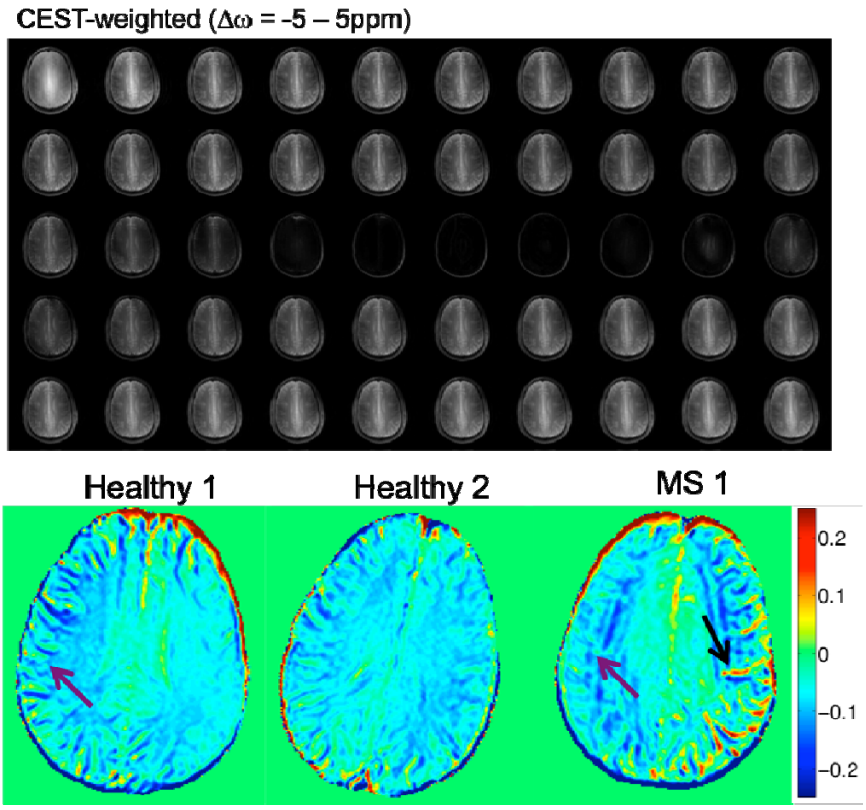

Figure 3: (top) example GluCEST-weighted images as a function of offset frequency (bottom) comparison of GluCEST maps for two healthy volunteers and one MS patient. Note the apparent differences between the MS patient and healthy volunteers (black and magenta arrows)

impairment. First, it can be seen that the GluCEST maps show excellent contrast between WM and GM, with the GM having higher GluCEST signal than the WM (expected). What is exciting to note (and in general, part of Task 5) is the visual differences between the patient and the two controls shown here. The MS patient shows elevated GluCEST signal (black arrow) on the left side, but apparently diminished GluCEST signal in the right cortical GM (magenta arrow) compared to healthy subject 1 (magenta arrow). This seems to indicate, at least at the early stages, that GluCEST is detecting cortical GM differences between healthy and MS patients.

As with the APT CEST, we examined the entire 20 healthy control cohort in comparison to the MS case and Figure 4A shows the average GluCEST spectra derived from GM and WM in healthy patients (blue and black, respectively) compared to the segmented GM in the MS case (red). It can be seen that the spectral quality is high and there is visual difference between the spectra for healthy and MS GM. Further, we analyzed the histogram of GluCEST signals for all GM voxels in all healthy volunteers and compared that to the 1 MS patient clinically diagnosed with cognitive challenges (Figure 4B). As with the APT CEST, it can be seen that the MS patient shows a downward trend compared to the healthy volunteer indicating the possibility of being sensitive to cortical GM pathology, which we will study in detail in Task 5. When we started this project, we decided against an "all-in-one" CEST acquisition scheme and rather have deployed two CEST acquisitions. One sensitive to APT (and apparently myoinositol) and one sensitive to glutamate. From Figure 4B, and in comparison to Figure 2B, the histograms from the APT-CEST analysis at Δω = 3.0ppm (glutamate) show now difference between healthy controls and the 1 MS patient, however, when utilizing the GluCEST acquisition, in the same patient, a difference can be appreciated. The rationale for this is

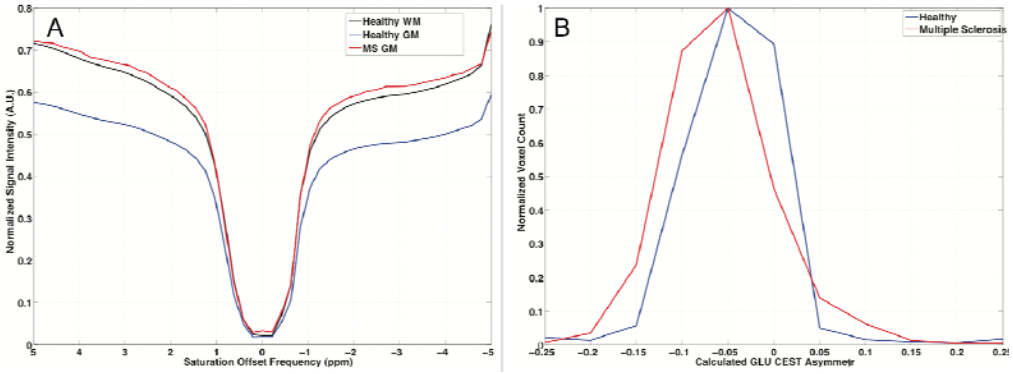

Figure 4: (A) Average GluCEST spectra for WM and GM in healthy (blue black) and MS patient (red) GM. (B) Histogram analysis shows that the MS has a downward shift of the GluCEST signal compared to the healthy volunteer (blue)

that the sensitivity to exchanging species is determined by the power of the RF CEST saturation. For the APT, the exchange rate is on the order of 20-100Hz, whereas for glutamate amines, the exchange rate is faster (50-200Hz). Thus, to be maximally sensitive to both, two separate pulse powers are necessary. We discovered this as part of Task 2 in the phantoms and are proud to note that it was the right choice going forward.

Quantitative Magnetization Transfer (qMT) analysis and results

High-resolution selective inversion recovery (SIR) qMT was performed in the same cohort as for CEST and analyzed according to (10) and given in Appendix 3. In short, an inversion recovery MRI sequence was performed using a modified inversion pulse that is relatively insensitive to B1 and B0 inhomogeneities. The inversion times were selected to sample the bi-exponential recovery known to exist when magnetization transfer is present. For every voxel, the SIR signal equation was fit to the recovery curve and the exchange rate (kmf), pool size ratio (PSR) and longitudinal relaxation time (R1f) was fit. Appendix 3 provides the manuscript that contains details of the pulse sequence, and fitting method.

Here we report the initial analyses and results from the newly deployed method. Figure 5, left panel shows the PSR, R1f, and kmf maps from a representative healthy volunteer and one patient with MS and concomitant cognitive impairment. From the PSR maps, it can be seen the high level of discrimination between WM (yellow/orange) and GM (blue) which agrees well with the R1f maps. Two things should be noted for the MS patient. First, the WM shows a globally decreased PSR which is indicative of demyelination across the entire slice, while the R1f and kmf maps do not show a similar pattern (discussed next). Secondly, when looking at the GM, it is not apparent that the patient and the control have different PSR values, yet MS patients are known

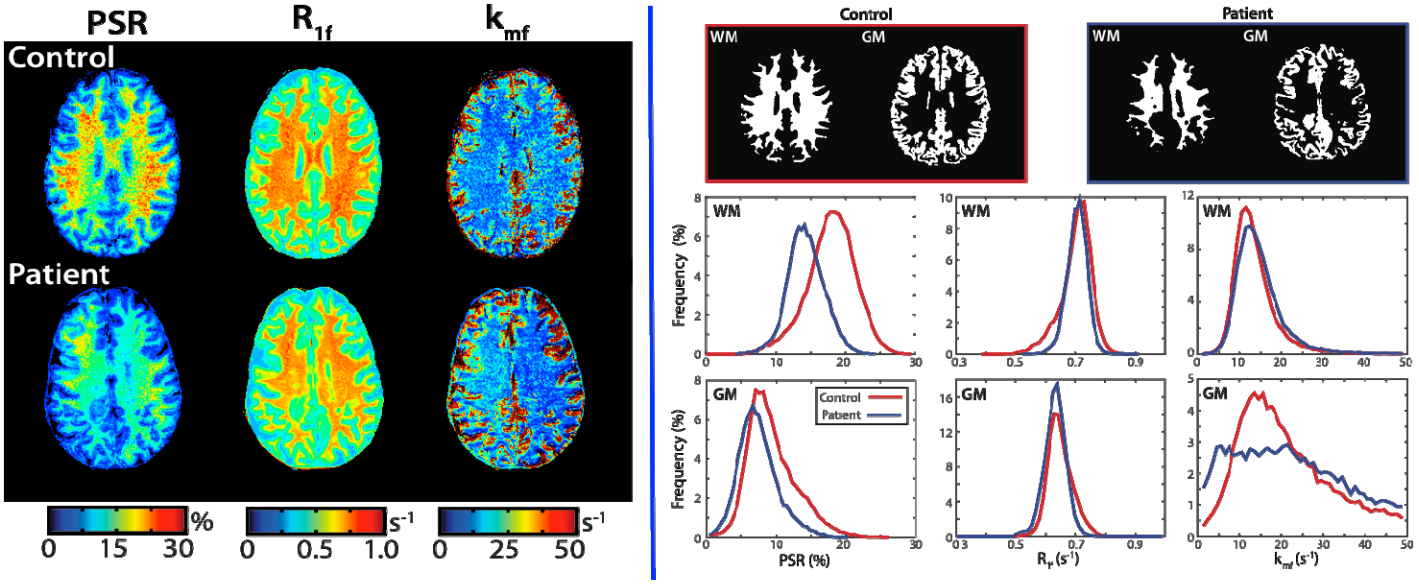

Figure 5: (left) qMT-derived maps for a healthy control (top) and MS patient (bottom). (right) segmentation results (top) and histogram analyses for the average healthy controls (red) and the MS patient (blue). Note the downward shift of the PSR for both WM and GM in this patient, while R1 and kmf are indistinguishable.

to have myelin loss in the GM. However, Figure 5, right panel, shows a histogram analysis of over the healthy volunteers (N = 20) and 1 MS patient. The top row shows the segmented WM and GM for an example healthy volunteer, and the bottom panels show the histograms for WM and GM for all of the qMT-derived indices. It can be seen again that for WM, the MS patient has a substantially downshifted PSR, normal R1f and kmf.

Importantly, however, in the GM, the patient also shows a small downshift of the PSR, while R1f and kmf are not markedly different (it should be noted that kmf showed some instabilities in this patient). This is important

to note in that one argument about MT imaging is that it is hypothesized that R1 drives the change in the MT effect moreso than does the macromolecular content. This figure shows that rather, in both WM and GM, the PSR is abnormal, but neither R1 nor kmf are indicating the sensitivity to WM and GM macromolecular pathology. Task 5 will explore this further when we examine a larger MS cohort.

fMRI analysis and results

In addition to the quantitative measures that have already been shown and at the advice of our mentor, Dr. Paul Newhouse, a neurocognition expert, we added 3 fMRI acquisitions to the MRI paradigm. Those three methods were an N-Back task, a Trail-making task, and a resting-state fMRI acquisition. The N-back and Trail-making tasks are important as they are also performed outside the MRI scanner, so we will be able to provide direct correlations between what is performed in the MRI and outside of the MRI. This further allows us to directly, and non-invasively probe cognitive performance in a manner that is not only unique, but it has not been performed in the MS population at 7T. We are encouraged by the initial results and wish to present those here. We performed the fMRI in 20 healthy volunteers and 1 MS patient at the time of this report. Figure 6 shows a direct comparison of the N-back 3 (left panels) and the Trail-making (right panels) for a single healthy volunteer (top panels) and a patient with MS (bottom panels). As it can be seen, at the same significance threshold, there are activation differences between the healthy volunteer and the MS patient. These are especially noted for areas in the superior cortex where working memory is targeted. A greater confidence will be gained with a group analysis, but this will be reserved for Task 5.

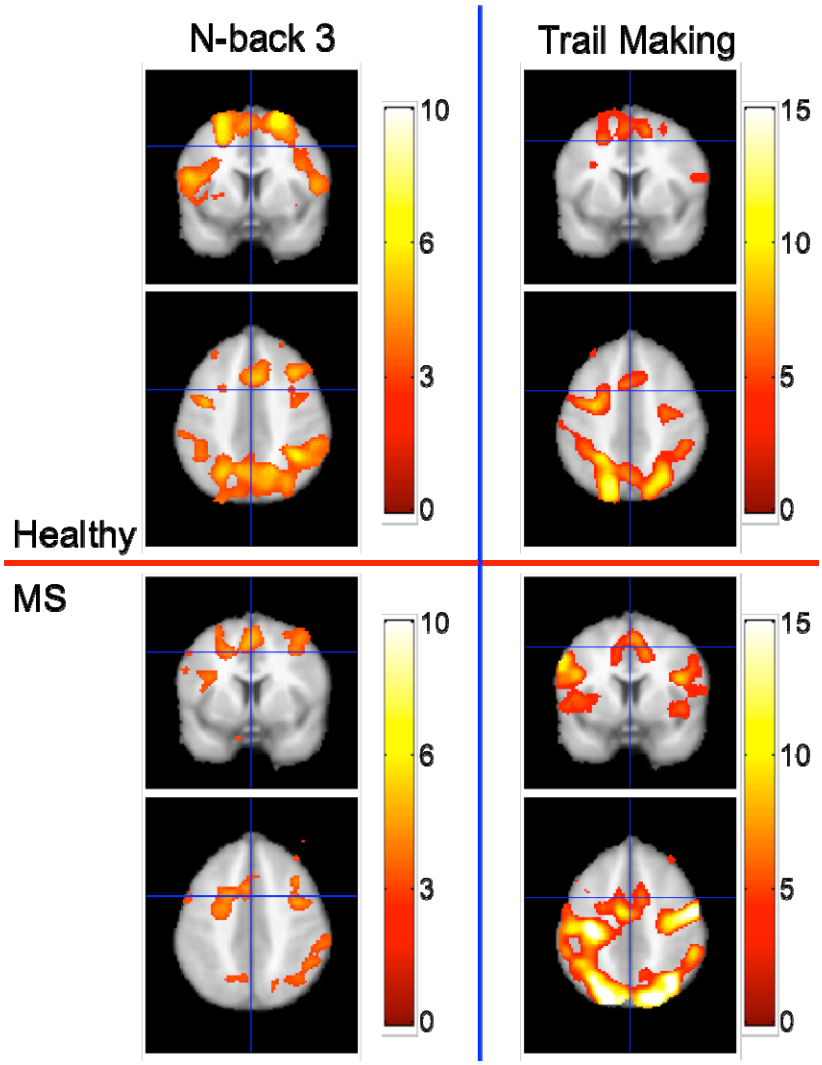

Figure 6 (left) N-back 3 and (right) Trail-making fMRI activation patterns in a healthy (top panels) volunteer and one patient with MS (bottom panels). Note for the N-back, there is less activation in the MS patient, where as for the Trail-making task, there are greater areas of activation.

Discussion of Task 4

We are pleased with the quality of data that has been generated and are actively enrolling healthy volunteer sand patients with MS. We have scanned 20 healthy volunteers, and 4 MS patients to this point, and have had 8 healthy volunteers return for a 2nd visit. We are slightly behind the enrollment expectation, but this is in large part due to the ground work necessary to start the human studies. We are, however, encouraged that because of this extensive focus on sequence optimization, that the data quality remains superb in all subjects. We have scheduled the remainder of the healthy subjects, developed a robust pipeline for analysis, and have shown initial success in implementing these acquisitions in patients with MS. We expect no delays in finalizing enrollment and will continue with reproducibility analysis from which we can gauge the level of expected deviation from normal in patients with MS.

Task 5 – Implementation in Patients with MS and concomitant cognitive impairment
The objective of this task is to deploy, and analyze the MRI acquisitions in patients with MS.

We have implemented the MRI paradigm in 4 patients with MS and expect no delays in enrollment for the remainder of the MS patients. The details of preliminary results are given in Task 4 with the goal of comparing both image quality, and quantitative differences. We have nothing else to report for Task 5 at the time of this annual report.

Task 6 – Cross-sectional analysis of derived indices between patients with MS and healthy volunteers and correlation with clinical measures of cognitive impairment derived from the Minimal Assessment of Cognitive Function in MS (MACFIMS)

The objective of this task is to compare quantitative MRI indices across cohorts, implement neuropsychiatric evaluations in both healthy and MS patient cohorts, and derive correlations with quantitative MR indices.

Neuropsychiatric Assessment Battery (Outside MRI Scanner)
In collaboration with Dr. Paul Newhouse, we have decided to additionally obtain neuropsychiatric evaluations in healthy volunteers in addition to patients with MS. This will provide us with a greater understanding of the variance across cohorts. Therefore, we have obtained neuropsychiatric data using the paradigm below in 20 healthy volunteers (8 repeats) and 4 MS patients.

Tasks - Outside the scanner and BEFORE coming to Vanderbilt
Questionnaire and survey already developed in REDCap to be completed at home and in a calm environment. These surveys will collect data related to baseline mood, anxiety, and cognitive profile.

Tasks - Outside the scanner at Vanderbilt (< 1 hour total)
- Short measure of day-of mood/anxiety
- N-back test (2-back or 3-back): measures working memory
- PASAT: measures working memory
- Trail making test (both A and B): measures planning/executive function
- "Black Box" (choice reaction time, critical flicker fusion; pre-scan and post-scan): measures processing speed/reaction time
- *Buschke selective reminding test (8 trials): measures include encoding and long-term memory
- Digit Symbol Substitution Test/DDST: measures visual memory
- Posner cueing task: measures attentional shift

KEY RESEARCH ACCOMPLISHMENTS:

1. Developed a Chemical Exchange Saturation Transfer (CEST) simulation pipeline to model the effects of glutamate, amide proton transfer, and myoinositol in the gray matter (GM) at 7T. These simulations reflect contributions from the metabolite of interest, the magnetization transfer (MT) effect, and the direct water saturation.
2. Developed a quantitative magnetization transfer (qMT) simulation pipeline to model the effects of macromolecular concentration of the white matter (WM) and GM in healthy tissue and tissue impacted by multiple sclerosis (MS). This pipeline incorporates modeling of the semisolid fraction while taking into account relaxation times (T1 and T2) changes that are known to occur in each cohort.
3. Phantoms have been created that attempt to model the in vivo scenario. That is, they have varied concentration of metabolite and concomitant concentration of semi-solid components (MT) at constant pH. These phantoms include: glutamate, myoinositol, glycogen, bovine serum albumin (BSA), and agarose. These phantoms can be leveraged for greater understanding of the in vivo results

4. Developed and optimized a set of novel MRI acquisition strategies to study the CEST effects of glutamate, myoinositol, amide protons, taking into account corrections for B1 and B0 inhomogeneities. These have been deployed in vivo.
5. Developed and optimized a high-resolution ($1mm^2$ in-plane resolution) qMT acquisition that is of sufficient resolution to assess cortical GM and juxtacortical WM in healthy and MS cohorts.
6. Developed a multi-modal motion-correction, coregistration and WM/GM/CSF segmentation strategy that not only maps the confidence of the measurements made in small structures, but also puts all acquisitions in the same space for descriptive statistics on each cohort.
7. Implemented a set of fMRI experiments to assess working memory and resting-state fluctuations in patients as compared to healthy controls. This will work in conjunction with item #8: neuropsychiatric evaluation
8. Created a detailed neuropsychiatric evaluation paradigm for assessing cognitive impairment that can be performed outside of the scanner environment and can be leveraged for correlation testing in the final year of this project.
9. In summary, we have developed, optimized, and deployed a multi-parametric, multi-modal MRI toolkit to assess neurochemical, macromolecular, functional, and structural changes in vivo at 7T. Additionally, we have developed a detailed neuropsychiatric evaluation paradigm to utilize for comparisons across cohorts, which can be further extended to any MRI study of cognitive impairment.

CONCLUSION:

We have concluded the first year of this project and have many significant contributions to report. First, we have for the first time, developed a battery of quantitative MRI methods that are of sufficient resolution and sensitivity to characterize cortical gray matter in healthy volunteers and patients with multiple sclerosis. To this end, we have a < 1 hour exam card that can be deployed on any 7T scanner that can investigate neurochemical composition, macromolecular/myelin deficiency, and functional impairment in a patient cohort. Additionally, we have generated data that suggests that there are differences between healthy volunteers and patients with MS, while expected, has yet to be shown because lower MRI field strengths have insufficient sensitivities to these macromolecules and neurochemicals, and insufficient resolution to study only gray matter. We have additionally partnered with a neurocognitive expert, and, with his help, developed a novel neuropsychiatric battery to assess cognition in MS. We understand that these techniques, while not novel, have not been implemented in patients with MS, and may provide evidence for greater scope in any patient with neurocognitive decline. We have studied 20 healthy volunteers and a handful of MS patients to this point and will expand the patient and control enrollment in year 2. We have finally, developed a pipeline for analysis that requires minimal human interaction and will deploy this for real-time analysis in year 2. It is important to note, however, that while these techniques are currently being explored for use at 7T, in year 2, we will develop a lower field, and thus, significantly more clinically relevant, set of exams that will provide a similar MRI toolkit. Lastly, the exam as developed here is not specific for MS and can be implemented in a wide range of patients and volunteers to explore the neurochemistry, functional processing, and macromolecular composition of cortical gray matter.

PUBLICATIONS, ABSTRACTS, AND PRESENTATIONS:

1. **Lay Press**: Nothing to report
2. **Peer-Reviewed Scientific Journals**: Nothing to report
3. **Invited Articles**: Nothing to report
4. **Abstracts**: 7 abstracts to the International Society for Magnetic Resonance in Medicine (ISMRM) annual conference have been prepared and will be submitted in Q1Y2 (November 12, 2014 deadline)

INVENTIONS, PATENTS AND LICENSES:

Nothing to Report

REPORTABLE OUTCOMES:

1. High-resolution, optimized 7T MRI acquisition strategies (so-called Exam Card in Philips language) to quantitatively evaluate the macromolecular, metabolic, functional, and structural characteristics that can (and currently is) be implemented in healthy controls and any patient cohort. A complete listing of the MRI acquisition paradigm (Exam Card) is given in Appendix 1.
2. Assessment of the reproducibility and stability of each measurement over time is currently ongoing.
3. A complete set of neuropsychiatric assessments, some of which are completely novel in patients with MS
4. Analysis pipeline for generation of quantitative MRI-derived indices. The pipeline includes motion correction, multi-modal image co-registration, and WM/GM/CSF segmentation along with generation of quantitative indices for further statistical comparisons.
5. A CEST simulation GUI for further studies of the CEST effect in vivo.
6. Collection of experiments, simulations, and phantom studies that have provided evidence for the minimal resolution attainable while maximizing sensitivity to change in patient populations.
7. Complete set of MRI and neuropsychiatric data in 20 healthy volunteers (with 8 additional repeat visits) and 4 patients with MS and clinically confirmed cognitive impairment. These data are summarized in the Overall Project Summary.

OTHER ACHIEVEMENTS:

1. Because of the nature of the experiments performed as a part of this grant, that is to implement the highest resolution quantitative MRI at 7T in WM and GM of healthy participants and MS patients, we have been able to extend these tools to the spinal cord, which has significant impact and scope for patients with other forms of neurological injury. One manuscript (*Dula AN, Pawate S, Dethrage LM, Conrad BN, Barry RL, Smith SA. CEST of the Cervical Spinal Cord at 7 Tesla. Submitted to NMR in Biomed on 30-Sept-2014*) has already been submitted on the results from this extension to other parts of the body.
2. The phantoms and simulations that were created are not MRI field strength dependent. Therefore, we have changed the simulations to study the impact of transitioning to a lower-field strength (i.e. 3T) for greater clinical implementation. We have begun to study the sensitivity for 3T utilization. This is critical, as it was noted in our initial application, that 7T MRI scanners are not directly clinically impactful. Thus, we have been able to create an MRI acquisition strategy at lower field strength which will be deployed in year 2. We are excited about the possibility of reaching a greater clinical community with the studies in year 2 at 3T.
3. From the preliminary results generated in the first year of this award, Dr. Pawate (co-investigator) is preparing a grant submission to the National Multiple Sclerosis Society in February 2015 to study cerebral changes in primary progressive MS (PPMS) patients.

REFERENCES: *List all references pertinent to the report using a standard journal format (i.e. format used in Science, Military Medicine, etc.)*

1. Jones CK, Polders D, Hua J, Zhu H, Hoogduin HJ, Zhou J, Luijten P, van Zijl PC. In vivo three-dimensional whole-brain pulsed steady-state chemical exchange saturation transfer at 7 T. Magn Reson Med 2012;67(6):1579-1589.3291747
2. Zaiss M, Schmitt B, Bachert P. Quantitative separation of CEST effect from magnetization transfer and spillover effects by Lorentzian-line-fit analysis of z-spectra. J Magn Reson 2011;211(2):149-155
3. Woessner DE, Zhang S, Merritt ME, Sherry AD. Numerical solution of the Bloch equations provides insights into the optimum design of PARACEST agents for MRI. Magn Reson Med 2005;53(4):790-799
4. Morrison C, Stanisz G, Henkelman RM. Modeling magnetization transfer for biological-like systems using a semi-solid pool with a super-Lorentzian lineshape and dipolar reservoir. Journal of magnetic resonance Series B 1995;108(2):103-113
5. Michaeli S, Garwood M, Zhu XH, DelaBarre L, Andersen P, Adriany G, Merkle H, Ugurbil K, Chen W. Proton T2 relaxation study of water, N-acetylaspartate, and creatine in human brain using Hahn and Carr-Purcell spin echoes at 4T and 7T. Magn Reson Med 2002;47(4):629-633
6. Rooney WD, Johnson G, Li X, Cohen ER, Kim SG, Ugurbil K, Springer CS, Jr. Magnetic field and tissue dependencies of human brain longitudinal 1H2O relaxation in vivo. Magn Reson Med 2007;57(2):308-318
7. Hua J, Jones CK, Blakeley J, Smith SA, van Zijl PC, Zhou J. Quantitative description of the asymmetry in magnetization transfer effects around the water resonance in the human brain. Magn Reson Med 2007;58(4):786-793.3707117
8. Cai K, Haris M, Singh A, Kogan F, Greenberg JH, Hariharan H, Detre JA, Reddy R. Magnetic resonance imaging of glutamate. Nature medicine 2012;18(2):302-306.3274604
9. Cai K, Singh A, Roalf DR, Nanga RP, Haris M, Hariharan H, Gur R, Reddy R. Mapping glutamate in subcortical brain structures using high-resolution GluCEST MRI. NMR in biomedicine 2013;26(10):1278-1284.3999922
10. Dortch RD, Moore J, Li K, Jankiewicz M, Gochberg DF, Hirtle JA, Gore JC, Smith SA. Quantitative magnetization transfer imaging of human brain at 7 T. NeuroImage 2013;64:640-649.3625658
11. Jones CK, Huang A, Xu J, Edden RA, Schar M, Hua J, Oskolkov N, Zaca D, Zhou J, McMahon MT, Pillai JJ, van Zijl PC. Nuclear Overhauser enhancement (NOE) imaging in the human brain at 7T. NeuroImage 2013;77:114-124.3848060

APPENDICES

Appendix 1

Philips MRI Protocol Dump

Created on

10/28/2014 10:40:51 AM

Comment

Created by ExamCard_to_XML with inputs: "E:\Export\20141021 CEST fMRI.ExamCard" on system (Vanderbilt University :: 192.168.71.10)

Software Stream

3.2.1.0

Expand All | Collapse All

(2) (1) (13)

Hospital (2)

20141021 CEST fMRI (13) 52:37.4

- SCOUT SHC32 00:28.7
- WIP MTX SENSE 32ch 01:28.9
- T1_3D_TFE_iso1.25mm_s2.5s SENSE_Sagittal 02:12.2
- CEST_interspersed_3uT 09:09.6
- CEST_Reddy_GluCEST 11:37.0
- B1_Reddy_multiAngle 01:42.0
- B0_Reddy_mulitecho 00:03.9
- qMT High Res 02:38.7
- FMRI_RESTINGSTATE 08:34.0
- FMRI_TRAILMAKING 04:14.0
- FMRI_nback 08:30.0
- T1_3D_TFE_quantGeo 00:55.7
- T2star_multiEcho 01:02.7

{B1860723-4F8F-476e-8075-D42C65706693} (0)

Hospital (2) | 20141021 CEST fMRI (13) 52:37.4 | SCOUT SHC32 00:28.7

INFO PAGE	
Total scan duration	00:28.7
Rel. signal level (%)	100
Act. TR/TE (ms)	7.8 / 4.9
ACQ matrix M x P	256 x 128
ACQ voxel MPS (mm)	0.98 / 1.95 / 10.0
REC voxel MPS (mm)	0.98 / 0.98 / 10.0
Scan percentage (%)	50
TFE shots	2
TFE dur. shot / acq (ms)	1062.9 / 501.9
TFE shot interval (ms)	1063.369
Min. TI delay	287.8819
Act. WFS (pix) / BW (Hz)	3.513 / 288.4
Min. WFS (pix) / Max. BW (Hz)	1.297 / 781.3
Min. TR/TE (ms)	7.8 / 2.8
RF avg power computed (W)	2.744635
SAR / head	< 100 %
Whole body / level	< 0.1 W/kg / normal
B1 rms	1.32 uT
PNS / level // VUIIS : dortch :	35 % / normal
Sound Pressure Level (dB)	26.85212
MOTION	
Cardiac synchronization	no
Heart rate > 250 bpm	no
Respiratory compensation	no
Navigator respiratory comp	no
Flow compensation	no
fMRI echo stabilisation	no
Motion smoothing	no
NSA	1
DYN/ANG	
Angio / Contrast enh.	no
Quantitative flow	no
Manual start	no
+Abuse dynamic loop	no
Dynamic study	no
Arterial Spin labeling	no
POST/PROC	
Preparation phases	auto
Interactive F0	no
SENSE ref. scan	no
SmartPlan survey	no
B0 field map	no
B1 field map	no
MIP/MPR	no
Images	M, no, no, no
Autoview image	M
Calculated images	no, no, no, no
Reference tissue	Grey matter
Preset window contrast	soft
Reconstruction mode	real time
Save raw data	no
Hardcopy protocol	no
Ringing filtering	rectangular
Geometry correction	default

GEOMETRY	
Multi-transmit	no
Nucleus	H1
Coil selection 1	RX-Intf-1
Xmit Coil selection	MTX-Volume-T/R
User def elem sel	no
element selection	All
connection	conn-A
Coil selection 2	RX-Intf-2
element selection	All
Dual coil	yes
Multi coil	no
CLEAR	no
FOV FH (mm)	250
AP (mm)	250
stack RL (mm)	50
Voxel size FH (mm)	0.9765625
AP (mm)	1.953125
Slice thickness (mm)	10
Recon voxel size (mm)	0.9765625
Fold-over suppression	no
Reconstruction matrix	256
SENSE	no
k-t BLAST	no
Stacks	3
current	A
type	parallel
slices	3
slice gap	user defined
gap (mm)	10
slice orientation	sagittal
fold-over direction	AP
fat shift direction	F
Slice scan order	default
Stack scan order	ascend
Move table per stack	no
Stack alignment	no
Stack display order	no
PlanAlign	no
REST slabs	0
Catheter tracking	no
Interactive positioning	no
Allow table movement	no
OFFC/ANG	
Stacks	3
current	A
Stack Offc. AP (P=+mm)	0
RL (L=+mm)	0
FH (H=+mm)	0
Ang. AP (deg)	0
RL (deg)	0
FH (deg)	0

CONTRAST	
Scan type	Imaging
Scan mode	M2D
technique	FFE
+ ZOOM	no
Contrast enhancement	T1
Acquisition mode	cartesian
Fast Imaging mode	TFE
shot mode	multishot
TFE factor	64
startup echoes	default
+TFE followup echoes	0
shot interval	shortest
profile order	linear
Echoes	1
partial echo	no
shifted echo	no
TE	in-phase
(ms)	4.93426
Flip angle (deg)	15
TR	shortest
Halfscan	no
Water-fat shift	user defined
(pixels)	3.5
Shim	default
mDIXON	no
Fat suppression	no
Water suppression	no
TFE prepulse	invert
slice selection	no
shared	no
delay	user defined
(ms)	800
PSIR	no
+inv pulse type	+default
MTC	no
T2prep	no
Research prepulse	no
Diffusion mode	no
Elastography mode	no
SAR mode	high
B1 mode	default
SAR Patient data	auto
PNS mode	low
Gradient mode	default
SofTone mode	no

Hospital (2) | 20141021 CEST fMRI (13) 52:37.4 | WIP MTX SENSE 32ch 01:28.9

INFO PAGE	
Total scan duration	01:28.9
Rel. signal level (%)	100
Act. TR/TE (ms)	8.0 / 0.75
ACQ matrix M x P	96 x 75
ACQ voxel MPS (mm)	5.52 / 7.07 / 6.00
REC voxel MPS (mm)	5.52 / 5.52 / 3.00
Scan percentage (%)	78.125
Packages	1
Act. WFS (pix) / BW (Hz)	0.489 / 2071.3
Min. WFS (pix) / Max. BW (Hz)	0.486 / 2083.3
RF avg power computed (W)	0.05085949
SAR / head	< 2 %
Whole body / level	0.0 W/kg / normal
B1 rms	0.18 uT
PNS / level // VUIIS : dortch :	18 % / normal
Sound Pressure Level (dB)	27.92985
MOTION	
Cardiac synchronization	no
Heart rate > 250 bpm	no
Respiratory compensation	no
Navigator respiratory comp	no
Flow compensation	no
fMRI echo stabilisation	no
NSA	3
SMART	yes
DYN/ANG	
Angio / Contrast enh.	no
Quantitative flow	no
Manual start	no
+Abuse dynamic loop	no
Dynamic study	no
Arterial Spin labeling	no
POST/PROC	
Preparation phases	full
Interactive F0	no
SENSE ref. scan	yes
SmartPlan survey	no
B0 field map	no
B1 field map	no
MIP/MPR	no
Images	no, no, no, no
Autoview image	no
Calculated images	no, no, no, no
Reference tissue	White matter
Preset window contrast	soft
Reconstruction mode	immediate
Save raw data	no
Hardcopy protocol	no
Ringing filtering	default
Elliptical k-space shutter	default

GEOMETRY	
Multi-transmit	no
Nucleus	H1
Coil selection 1	RX-Intf-1
Xmit Coil selection	MTX-Volume-T/R
User def elem sel	no
element selection	All
connection	conn-A
Coil selection 2	RX-Intf-2
element selection	All
Dual coil	yes
Multi coil	yes
CLEAR	no
FOV FH (mm)	530
RL (mm)	530
stack AP (mm)	300
Voxel size FH (mm)	5.520833
RL (mm)	7.066667
AP (mm)	3
Recon voxel size (mm)	5.520833
Image shutter	yes
Fold-over suppression	no
Slice oversampling	default
RF select. FOS	no
Reconstruction matrix	96
SENSE	no
k-t BLAST	no
Overcontiguous slices	yes
Stacks	2
current	A slices
	100
slice orientation	coronal
fold-over direction	RL
fat shift direction	F
Chunks	1
Stacks as packages	no
Move table per stack	no
Stack alignment	no
Stack display order	no
PlanAlign	no
REST slabs	0
Catheter tracking	no
Interactive positioning	no
Allow table movement	no
OFFC/ANG	
Stacks	2
current	A
Stack Offc. AP (P=+mm)	11.5916
RL (L=+mm)	-3.434925
FH (H=+mm)	4.208135
Ang. AP (deg)	0
RL (deg)	0
FH (deg)	0

CONTRAST	
Scan type	Imaging
Scan mode	3D
technique	FFE
loop order	zy_order
+ ZOOM	no
Contrast enhancement	T1
Acquisition mode	cartesian
Fast Imaging mode	none
3D non-selective	no
Echoes	1
partial echo	no
shifted echo	no
TE	shortest
Flip angle (deg)	1
TR	shortest
Halfscan	no
Water-fat shift	minimum
Shim	default
mDIXON	no
Fat suppression	no
Water suppression	no
MTC	no
Research prepulse	no
Diffusion mode	no
Elastography mode	no
SAR mode	high
B1 mode	default
SAR Patient data	auto
PNS mode	low
Gradient mode	default
SofTone mode	no

Hospital (2) | 20141021 CEST fMRI (13) 52:37.4 | T1_3D_TFE_iso1.25mm_s2.5s SENSE_Sagittal 02:12.2

INFO PAGE	
Total scan duration	02:12.2
Rel. signal level (%)	100
Act. TR/TE (ms)	2.8 / 1.32
ACQ matrix M x P	204 x 204
ACQ voxel MPS (mm)	1.25 / 1.25 / 1.25
REC voxel MPS (mm)	1.14 / 1.14 / 1.25
Scan percentage (%)	100
TFE shots	30
TFE dur. shot / acq (ms)	1669.4 / 716.5
Min. TI delay	381.0045
Act. WFS (pix) / BW (Hz)	0.579 / 1750.7
Min. WFS (pix) / Max. BW (Hz)	0.575 / 1763.2
RF avg power computed (W)	0.8993402
SAR / head	< 33 %
Whole body / level	0.0 W/kg / normal
B1 rms	0.76 uT
PNS / level // VUIIS : dortch :	57 % / normal
Sound Pressure Level (dB)	37.43258
MOTION	
Cardiac synchronization	no
Heart rate > 250 bpm	no
Respiratory compensation	no
Navigator respiratory comp	no
Flow compensation	no
fMRI echo stabilisation	no
Motion smoothing	no
NSA	1
DYN/ANG	
Angio / Contrast enh.	no
Quantitative flow	no
CENTRA	no
Manual start	no
+Abuse dynamic loop	no
Dynamic study	no
Arterial Spin labeling	no
POST/PROC	
Preparation phases	auto
Interactive F0	no
SENSE ref. scan	no
SmartPlan survey	no
B0 field map	no
B1 field map	no
MIP/MPR	no
Images	M, no, no, no
Autoview image	M
Calculated images	no, no, no, no
Reference tissue	Grey matter
Preset window contrast	soft
Reconstruction mode	immediate
Save raw data	no
Hardcopy protocol	no
Ringing filtering	rectangular
Geometry correction	default
Elliptical k-space shutter	default

GEOMETRY	
Multi-transmit	no
Nucleus	H1
Coil selection 1	RX-Intf-1
Xmit Coil selection	MTX-Volume-T/R
User def elem sel	no
element selection	All
connection	conn-A
Coil selection 2	RX-Intf-2
element selection	All
Dual coil	yes
CLEAR	yes
body tuned	yes
FOV FH (mm)	256
AP (mm)	256
RL (mm)	172.5
Voxel size FH (mm)	1.25
AP (mm)	1.254902
RL (mm)	1.25
Recon voxel size (mm)	1.142857
Fold-over suppression	no
Slice oversampling	default
RF select. FOS	no
Reconstruction matrix	224
SENSE	yes
P reduction (AP)	2
P os factor	1
S reduction (RL)	2
k-t BLAST	no
Overcontiguous slices	no
Stacks	1
slices	138
slice orientation	sagittal
fold-over direction	AP
fat shift direction	F
Chunks	1
PlanAlign	no
REST slabs	0
Catheter tracking	no
Interactive positioning	no
Allow table movement	no
OFFC/ANG	
Stacks	1
Stack Offc. AP (P=+mm)	11.5916
RL (L=+mm)	-3.434925
FH (H=+mm)	4.208135
Ang. AP (deg)	0
RL (deg)	0
FH (deg)	0

CONTRAST	
Scan type	Imaging
Scan mode	3D
technique	FFE
+ ZOOM	no
Contrast enhancement	T1
Acquisition mode	cartesian
Fast Imaging mode	TFE
3D non-selective	no
shot mode	multishot
TFE factor	256
3D free factor	no
startup echoes	default
+TFE followup echoes	0
shot interval	user defined
(ms)	4500
profile order	linear
turbo direction	radial
CENTRA (spiral)	no
Echoes	1
partial echo	no
shifted echo	no
TE	shortest
Flip angle (deg)	7
TR	shortest
Halfscan	no
Water-fat shift	minimum
Shim	auto
mDIXON	no
Fat suppression	no
Water suppression	no
TFE prepulse	invert
slice selection	no
delay	user defined
(ms)	1300
PSIR	no
+inv pulse type	+B1 opt (low BW)
MTC	no
T2prep	no
Research prepulse	no
Diffusion mode	no
Elastography mode	no
SAR mode	high
B1 mode	default
SAR Patient data	auto
PNS mode	low
Gradient mode	full control
max strength (mT/m)	33
max slew rate (T/m/s)	166

Hospital (2) | 20141021 CEST fMRI (13) 52:37.4 | CEST_interspersed_3uT 09:09.6

INFO PAGE	
Total scan duration	09:09.6
Rel. signal level (%)	100
Act. TR/TE (ms)	65 / 7.2
Dyn. scan time	00:08.579
Time to k0	00:04.7
ACQ matrix M x P	160 x 148
ACQ voxel MPS (mm)	1.50 / 1.62 / 10.0
REC voxel MPS (mm)	0.94 / 0.94 / 5.00
Scan percentage (%)	92.77109
Act. WFS (pix) / BW (Hz)	8.715 / 116.3
BW in EPI freq. dir. (Hz)	1230.8
Min. WFS (pix) / Max. BW (Hz)	8.664 / 117.0
Min. TR/TE (ms)	54 / 5.9
RF avg power computed (W)	1.351341
SAR / head	< 49 %
Whole body / level	< 0.1 W/kg / normal
B1 rms	0.93 uT
PNS / level // VUIIS : dortch :	50 % / normal
Sound Pressure Level (dB)	25.24222
MOTION	
Cardiac synchronization	no
Heart rate > 250 bpm	no
Respiratory compensation	no
Navigator respiratory comp	no
Flow compensation	no
fMRI echo stabilisation	no
NSA	1
DYN/ANG	
Angio / Contrast enh.	no
Quantitative flow	no
Manual start	no
+Abuse dynamic loop	no
Dynamic study	individual
dyn scans	64
recon multiplier	1
dyn scan times	shortest
FOV time mode	default
dummy scans	0
immediate subtraction	no
fast next scan	no
synch. ext. device	no
MTC	no
dyn stabilization	no
prospect. motion corr.	no
Keyhole	no
Arterial Spin labeling	no
POST/PROC	
Preparation phases	sameprep
Interactive F0	no
SENSE ref. scan	no
SmartPlan survey	no
B0 field map	no
B1 field map	no
MIP/MPR	no
Images	M, no, no, no
Autoview image	M
Calculated images	no, no, no, no
Reference tissue	Grey matter
EPI 2D phase correction	no
Preset window contrast	soft
Reconstruction mode	real time
reuse memory	no
Save raw data	no
Hardcopy protocol	no
Ringing filtering	rectangular
Geometry correction	default
Elliptical k-space shutter	default

GEOMETRY	
Multi-transmit	no
Nucleus	H1
Coil selection 1	RX-Intf-1
Xmit Coil selection	MTX-Volume-T/R
User def elem sel	no
element selection	All
connection	conn-A
Coil selection 2	RX-Intf-2
element selection	All
Dual coil	yes
CLEAR	yes
body tuned	no
FOV AP (mm)	240
RL (mm)	240
FH (mm)	165
Voxel size AP (mm)	1.5
RL (mm)	1.5
FH (mm)	5
Recon voxel size (mm)	0.9375
Fold-over suppression	no
Slice oversampling	default
RF select. FOS	no
Reconstruction matrix	256
SENSE	yes
P reduction (RL)	2
P os factor	1
S reduction (FH)	2
k-t BLAST	no
Overcontiguous slices	yes
Stacks	1
slices	33
slice orientation	transverse
fold-over direction	RL
fat shift direction	L
Chunks	1
PlanAlign	no
REST slabs	0
Catheter tracking	no
Interactive positioning	no
Allow table movement	no
OFFC/ANG	
Stacks	1
Stack Offc. AP (P=+mm)	-5.532147
RL (L=+mm)	-3.434925
FH (H=+mm)	35.45897
Ang. AP (deg)	0
RL (deg)	-5.457352
FH (deg)	0
Shim Size AP (mm)	180.7495
RL (mm)	134.1432
FH (mm)	114.2866
Offc. AP (P=+mm)	-1.87074
RL (L=+mm)	-3.660397
FH (H=+mm)	33.86363
Ang. AP (deg)	2.26406
RL (deg)	-6.580403
FH (deg)	4.637685

CONTRAST	
Scan type	Imaging
Scan mode	3D
technique	FFE
+ ZOOM	no
Contrast enhancement	T1
Acquisition mode	cartesian
Fast Imaging mode	EPI
3D non-selective	no
shot mode	multishot
EPI factor	7
epi direction	Y
Echoes	1
partial echo	no
shifted echo	no
TE	user defined
(ms)	7.2
Flip angle (deg)	5
TR	user defined
(ms)	65
Halfscan	no
Water-fat shift	minimum
Shim	volume
ShimAlign	no
mDIXON	no
Fat suppression	ProSet
pulse type	1331
Water suppression	no
MTC	+pulsed qMT/CEST
+Duration (ms)	25
+B1 Mode	constant
+Amp	3
+B1 Units	max amp. (uT)
+Pulses/TR	1
+Offset Mode	file
+Offset File	G:/patch/rf_offsets.txt
+Offset Units	ppm
+RF Shape	gauss_cest_mt
Research prepulse	no
Diffusion mode	no
Elastography mode	no
SAR mode	high
B1 mode	default
SAR Patient data	auto
PNS mode	low
Gradient mode	default
SofTone mode	no

Hospital (2) | 20141021 CEST fMRI (13) 52:37.4 | CEST_Reddy_GluCEST 11:37.0

INFO PAGE	
Total scan duration	11:37.0
Rel. signal level (%)	100
Act. TR/TE (ms)	5.6 / 2.7
Dyn. scan time	00:13.909
Time to k0	00:08.6
ACQ matrix M x P	128 x 126
ACQ voxel MPS (mm)	1.88 / 1.90 / 10.0
REC voxel MPS (mm)	0.94 / 0.94 / 10.0
Scan percentage (%)	98.4375
TFE shots	42
TFE dur. shot / acq (ms)	134.0 / 16.8
TFE shot interval (ms)	331.1945
Act. WFS (pix) / BW (Hz)	0.700 / 1446.8
Min. WFS (pix) / Max. BW (Hz)	0.649 / 1562.5
Min. TR/TE (ms)	4.0 / 1.36
RF avg power computed (W)	2.058919
SAR / head	< 75 %
Whole body / level	< 0.1 W/kg / normal
B1 rms	1.15 uT
PNS / level // VUIIS : dortch :	31 % / normal
Sound Pressure Level (dB)	17.13024
MOTION	
Cardiac synchronization	no
Heart rate > 250 bpm	no
Respiratory compensation	no
Navigator respiratory comp	no
Flow compensation	no
fMRI echo stabilisation	no
Motion smoothing	no
NSA	1
DYN/ANG	
Angio / Contrast enh.	no
Quantitative flow	no
Manual start	no
+Abuse dynamic loop	no
Dynamic study	individual
dyn scans	50
recon multiplier	1
dyn scan times	shortest
FOV time mode	default
dummy scans	0
immediate subtraction	no
fast next scan	no
synch. ext. device	no
MTC	no
dyn stabilization	no
prospect. motion corr.	no
Keyhole	no
Arterial Spin labeling	no
POST/PROC	
Preparation phases	sameprep
Interactive F0	no
SENSE ref. scan	no
SmartPlan survey	no
B0 field map	no
B1 field map	no
MIP/MPR	no
Images	M, no, no, no
Autoview image	M
Calculated images	no, no, no, no
Reference tissue	Grey matter
Preset window contrast	soft
Reconstruction mode	real time
reuse memory	no
Save raw data	no
Hardcopy protocol	no
Ringing filtering	rectangular
Geometry correction	default

GEOMETRY	
Multi-transmit	no
Nucleus	H1
Coil selection 1	RX-Intf-1
Xmit Coil selection	MTX-Volume-T/R
User def elem sel	no
element selection	All
connection	conn-A
Coil selection 2	RX-Intf-2
element selection	All
Dual coil	yes
CLEAR	yes
body tuned	no
FOV AP (mm)	240
RL (mm)	240
Voxel size AP (mm)	1.87
RL (mm)	1.87
Slice thickness (mm)	10
Recon voxel size (mm)	0.9375
Fold-over suppression	no
Reconstruction matrix	256
SENSE	no
k-t BLAST	no
Slice orientation	transverse
Fold-over direction	RL
Fat shift direction	P
PlanAlign	no
REST slabs	0
Catheter tracking	no
Interactive positioning	no
Allow table movement	no
OFFC/ANG	
Slice Offc. AP (P=+mm)	-4.247866
RL (L=+mm)	-3.434925
FH (H=+mm)	35.88707
Ang. AP (deg)	0
RL (deg)	-5.457352
FH (deg)	0
Shim Size AP (mm)	180.7495
RL (mm)	134.1432
FH (mm)	106.6376
Offc. AP (P=+mm)	-1.87074
RL (L=+mm)	-3.660397
FH (H=+mm)	33.86363
Ang. AP (deg)	2.26406
RL (deg)	-6.580403
FH (deg)	4.637685

CONTRAST	
Scan type	Imaging
Scan mode	2D
technique	FFE
+ ZOOM	no
Contrast enhancement	T1
Acquisition mode	cartesian
Fast Imaging mode	TFE
shot mode	multishot
TFE factor	3
startup echoes	default
+TFE followup echoes	0
shot interval	shortest
profile order	low_high
Echoes	1
partial echo	no
shifted echo	no
TE	user defined
(ms)	2.7
Flip angle (deg)	10
TR	user defined
(ms)	5.6
Halfscan	no
Water-fat shift	minimum
Shim	volume
ShimAlign	no
mDIXON	no
Fat suppression	no
Water suppression	no
TFE prepulse	no
MTC	+pulsed qMT/CEST
+Duration (ms)	10
+B1 Mode	constant
+Amp	4.25
+B1 Units	max amp. (uT)
+Pulses/TR	10
+Duty Cycle	0.9
+Offset Mode	baseline+range
+Min Offset	-5
+Max Offset	5
+Offset Units	ppm
+RF Shape	gauss_cest_mt
+Interpulse Spoiling	no
T2prep	no
Research prepulse	no
Diffusion mode	no
Elastography mode	no
SAR mode	moderate
B1 mode	default
SAR Patient data	auto
PNS mode	low
Gradient mode	default
SofTone mode	no

Hospital (2) | 20141021 CEST fMRI (13) 52:37.4 | B1_Reddy_multiAngle 01:42.0

INFO PAGE	
Total scan duration	01:42.0
Rel. signal level (%)	100
Act. TR (ms)	6000
Act. TE (ms)	12
Dyn. scan time	00:48.000
ACQ matrix M x P	128 x 120
ACQ voxel MPS (mm)	1.88 / 2.00 / 10.0
REC voxel MPS (mm)	0.94 / 0.94 / 10.0
Scan percentage (%)	93.75
Packages	1
Min. slice gap (mm)	10
WFS (pix) / BW (Hz)	1.986 / 510.1
TSE es / shot (ms)	12.0 / 180
TEeff / TEequiv (ms)	12 / 12
Min. TR (ms)	589
RF avg power computed (W)	0.2697158
SAR / head	< 10 %
Whole body / level	0.0 W/kg / normal
B1 rms	0.41 uT
PNS / level // VUIIS : dortch :	30 % / normal
Sound Pressure Level (dB)	16.02466
+Ref Pulse Shape	
+Ref Pulse Dur [msec]	
+Ref MAX Dephase	
+Ref MIN Dephase	
+Crusher b value	

MOTION	
Cardiac synchronization	no
Heart rate > 250 bpm	no
Respiratory compensation	no
Navigator respiratory comp	no
Flow compensation	no
Temporal slice spacing	default
Motion smoothing	no
NSA	1

DYN/ANG	
Manual start	no
+Abuse dynamic loop	flip angle diminish
Dynamic study	individual
dyn scans	2
recon multiplier	1
dyn scan times	shortest
FOV time mode	default
dummy scans	0
immediate subtraction	no
fast next scan	no
synch. ext. device	no
dyn stabilization	no
prospect. motion corr.	no
Keyhole	no
Arterial Spin labeling	no

POST/PROC	
Preparation phases	sameprep
Interactive F0	no
SENSE ref. scan	no
SmartPlan survey	no
B0 field map	no
B1 field map	no
MIP/MPR	no
Images	M, no, no, no
Autoview image	M
Calculated images	no, no, no, no
Reference tissue	Grey matter
Preset window contrast	soft
Reconstruction mode	real time
reuse memory	no
Save raw data	no
Hardcopy protocol	no
Ringing filtering	rectangular
Geometry correction	default

GEOMETRY	
Multi-transmit	no
Nucleus	H1
Coil selection 1	RX-Intf-1
Xmit Coil selection	MTX-Volume-T/R
User def elem sel	no
element selection	All
connection	conn-A
Coil selection 2	RX-Intf-2
element selection	All
Dual coil	yes
CLEAR	no
FOV AP (mm)	240
RL (mm)	240
FH (mm)	10
Voxel size AP (mm)	1.87
RL (mm)	1.87
Slice thickness (mm)	10
Recon voxel size (mm)	0.9375
Small FOV imaging	no
Fold-over suppression	no
Reconstruction matrix	256
SENSE	no
k-t BLAST	no
Stacks	1
type	parallel
slices	1
slice gap	user defined
gap (mm)	0
slice orientation	transverse
fold-over direction	RL
fat shift direction	P
Minimum number of packages	1
Slice scan order	default
PlanAlign	no
REST slabs	0
Catheter tracking	no
Interactive positioning	no
Allow table movement	no

OFFC/ANG	
Stacks	1
Stack Offc. AP (P=+mm)	-4.247866
RL (L=+mm)	-3.434925
FH (H=+mm)	35.88707
Ang. AP (deg)	0
RL (deg)	-5.457352
FH (deg)	0
Shim Size AP (mm)	180.7495
RL (mm)	134.1432
FH (mm)	106.6376
Offc. AP (P=+mm)	-1.87074
RL (L=+mm)	-3.660397
FH (H=+mm)	33.86363
Ang. AP (deg)	2.26406
RL (deg)	-6.580403
FH (deg)	4.637685

CONTRAST	
Scan type	Imaging
Scan mode	MS
technique	SE
+ ZOOM	no
Modified SE	no
+Optim ref/crush	no
Acquisition mode	cartesian
Fast Imaging mode	TSE
shot mode	multishot
TSE factor	15
startup echoes	0
+followup echoes	0
profile order	low_high
DRIVE	no
ultrashort	no
strong FID crushing	no
Echoes	1
partial echo	no
TE	user defined
(ms)	12
Flip angle (deg)	60
Refocusing control	no
TR	user defined
(ms)	6000
Halfscan	no
Water-fat shift	user defined
(pixels)	2
Shim	volume
ShimAlign	no
mDIXON	no
Fat suppression	no
Water suppression	no
Grad. rev. offres. supp.	no
BB pulse	no
MTC	no
T2prep	no
Research prepulse	no
Zoom imaging	no
Diffusion mode	no
Elastography mode	no
SAR mode	high
B1 mode	user defined
amplitude (uT)	9.5
SAR Patient data	auto
PNS mode	high
Gradient mode	default
SofTone mode	no

Hospital (2) | 20141021 CEST fMRI (13) 52:37.4 | B0_Reddy_mulitecho 00:03.9

INFO PAGE	
Total scan duration	00:03.9
Rel. signal level (%)	100
Act. TR/TE1/delta TE (ms)	53 / 3.4 / 3.9
ACQ matrix M x P	128 x 128
ACQ voxel MPS (mm)	1.88 / 1.88 / 10.0
REC voxel MPS (mm)	0.94 / 0.94 / 10.0
Scan percentage (%)	100
Act. WFS (pix) / BW (Hz)	2.824 / 358.8
Min. WFS (pix) / Max. BW (Hz)	0.649 / 1562.5
RF avg power computed (W)	2.058916
SAR / head	< 75 %
Whole body / level	< 0.1 W/kg / normal
B1 rms	1.15 uT
PNS / level // VUIIS : dortch :	46 % / normal
Sound Pressure Level (dB)	21.87152
MOTION	
Cardiac synchronization	no
Heart rate > 250 bpm	no
Respiratory compensation	no
Navigator respiratory comp	no
Flow compensation	yes
fMRI echo stabilisation	no
NSA	1
DYN/ANG	
Angio / Contrast enh.	no
Quantitative flow	no
Manual start	no
+Abuse dynamic loop	no
Dynamic study	no
Arterial Spin labeling	no
POST/PROC	
Preparation phases	sameprep
Interactive F0	no
SENSE ref. scan	no
SmartPlan survey	no
B0 field map	no
B1 field map	no
MIP/MPR	no
Images	M, R, I, no
Autoview image	M
Calculated images	no, no, no, no
Reference tissue	Grey matter
Preset window contrast	soft
Reconstruction mode	real time
Save raw data	yes
Hardcopy protocol	no
Ringing filtering	rectangular
Geometry correction	default

GEOMETRY	
Multi-transmit	no
Nucleus	H1
Coil selection 1	RX-Intf-1
Xmit Coil selection	MTX-Volume-T/R
User def elem sel	no
element selection	All
connection	conn-A
Coil selection 2	RX-Intf-2
element selection	All
Dual coil	yes
CLEAR	yes
body tuned	no
FOV AP (mm)	240
RL (mm)	240
Voxel size AP (mm)	1.87
RL (mm)	1.875
Slice thickness (mm)	10
Recon voxel size (mm)	0.9375
Fold-over suppression	no
Reconstruction matrix	256
SENSE	yes
P reduction (RL)	2
P os factor	1
k-t BLAST	no
Slice orientation	transverse
Fold-over direction	RL
Fat shift direction	P
PlanAlign	no
REST slabs	0
Catheter tracking	no
Interactive positioning	no
Allow table movement	no
OFFC/ANG	
Slice Offc. AP (P=+mm)	-4.247866
RL (L=+mm)	-3.434925
FH (H=+mm)	35.88707
Ang. AP (deg)	0
RL (deg)	-5.457352
FH (deg)	0
Shim Size AP (mm)	180.7495
RL (mm)	134.1432
FH (mm)	106.6376
Offc. AP (P=+mm)	-1.87074
RL (L=+mm)	-3.660397
FH (H=+mm)	33.86363
Ang. AP (deg)	2.26406
RL (deg)	-6.580403
FH (deg)	4.637685

CONTRAST	
Scan type	Imaging
Scan mode	2D
technique	FFE
+ ZOOM	no
Contrast enhancement	no
Acquisition mode	cartesian
Fast Imaging mode	none
Echoes	4
partial echo	no
shifted echo	no
TE first	shortest
echospacing	shortest
flyback	yes
Flip angle (deg)	65
TR	shortest
Halfscan	no
Water-fat shift	maximum
Shim	volume
ShimAlign	no
mDIXON	no
Fat suppression	no
Water suppression	no
MTC	no
Research prepulse	no
Diffusion mode	no
Elastography mode	no
SAR mode	moderate
B1 mode	default
SAR Patient data	auto
PNS mode	low
Gradient mode	default
SofTone mode	no

Hospital (2) | 20141021 CEST fMRI (13) 52:37.4 | qMT High Res 02:38.7

INFO PAGE	
Total scan duration	02:38.7
Rel. signal level (%)	100
Act. TR/TE (ms)	4.2 / 2.2
Dyn. scan time	00:11.251
Time to k0	00:07.0
ACQ matrix M x P	212 x 210
ACQ voxel MPS (mm)	1.00 / 1.01 / 2.00
REC voxel MPS (mm)	0.95 / 0.95 / 2.00
Scan percentage (%)	99.08257
TFE shots	12
TFE dur. shot / acq (ms)	233.8 / 225.8
TFE shot interval (ms)	3353.226
Act. WFS (pix) / BW (Hz)	1.142 / 887.5
Min. WFS (pix) / Max. BW (Hz)	1.133 / 894.1
RF avg power computed (W)	1.347757
SAR / head	< 49 %
Whole body / level	< 0.1 W/kg / normal
B1 rms	0.93 uT
PNS / level // VUIIS : dortch :	50 % / normal
Sound Pressure Level (dB)	29.07384

MOTION	
Cardiac synchronization	no
Heart rate > 250 bpm	no
Respiratory compensation	no
Navigator respiratory comp	no
Flow compensation	no
fMRI echo stabilisation	no
Motion smoothing	no
NSA	1

DYN/ANG	
Angio / Contrast enh.	no
Quantitative flow	no
CENTRA	no
Manual start	no
+Abuse dynamic loop	no
Dynamic study	individual
dyn scans	14
recon multiplier	1
dyn scan times	shortest
FOV time mode	default
dummy scans	0
immediate subtraction	no
fast next scan	no
synch. ext. device	no
MTC	no
dyn stabilization	no
prospect. motion corr.	no
Keyhole	no
Arterial Spin labeling	no

POST/PROC	
Preparation phases	auto
Interactive F0	no
SENSE ref. scan	no
SmartPlan survey	no
B0 field map	no
B1 field map	no
MIP/MPR	no
Images	M, R, I, no
Autoview image	M
Calculated images	no, no, no, no
Reference tissue	Grey matter
Preset window contrast	soft
Reconstruction mode	real time
reuse memory	no
Save raw data	no
Hardcopy protocol	no
Ringing filtering	rectangular
Geometry correction	default
Elliptical k-space shutter	default

GEOMETRY	
Multi-transmit	no
Nucleus	H1
Coil selection 1	RX-Intf-1
Xmit Coil selection	MTX-Volume-T/R
User def elem sel	no
element selection	All
connection	conn-A
Coil selection 2	RX-Intf-2
element selection	All
Dual coil	yes
CLEAR	yes
body tuned	no
FOV AP (mm)	212
RL (mm)	212
FH (mm)	10
Voxel size AP (mm)	1
RL (mm)	1
FH (mm)	2
Recon voxel size (mm)	1
Fold-over suppression	no
Slice oversampling	default
RF select. FOS	no
Reconstruction matrix	224
SENSE	yes
P reduction (RL)	2
P os factor	1
S reduction (FH)	1
k-t BLAST	no
Overcontiguous slices	no
Stacks	1
slices	5
slice orientation	transverse
fold-over direction	RL
fat shift direction	P
Chunks	1
PlanAlign	no
REST slabs	0
Catheter tracking	no
Interactive positioning	no
Allow table movement	no

OFFC/ANG	
Stacks	1
Stack Offc. AP (P=+mm)	-4.247866
RL (L=+mm)	-3.434925
FH (H=+mm)	35.88707
Ang. AP (deg)	0
RL (deg)	-5.457352
FH (deg)	0
Shim Size AP (mm)	180.7495
RL (mm)	134.1432
FH (mm)	106.6376
Offc. AP (P=+mm)	-1.87074
RL (L=+mm)	-3.660397
FH (H=+mm)	33.86363
Ang. AP (deg)	2.26406
RL (deg)	-6.580403
FH (deg)	4.637685

CONTRAST	
Scan type	Imaging
Scan mode	3D
technique	FFE
+ ZOOM	no
Contrast enhancement	T1
Acquisition mode	cartesian
Fast Imaging mode	TFE
3D non-selective	no
shot mode	multishot
TFE factor	54
3D free factor	no
startup echoes	user defined
(number)	0
+TFE followup echoes	0
shot interval	shortest
profile order	low_high
turbo direction	Y
Echoes	1
partial echo	no
shifted echo	no
TE	shortest
Flip angle (deg)	15
TR	shortest
Halfscan	no
Water-fat shift	minimum
Shim	PB-volume
ShimAlign	no
mDIXON	no
Fat suppression	no
Water suppression	no
TFE prepulse	no
MTC	+SIR
+pulse dur (ms)	5.5
+pulse shape	BRASORF
+offset (Hz)	0
+spoil amp (mT/m)	20
+spoil dur (ms)	2
+TFE Saturation	yes
+td Mode	constant
+td (ms)	2500
+ti (ms)	6, 10, 16, 26, 42, 68, 110, 178, 288, 468, 760, 1233, 2000, 8000, 2000, 10000, 1000
T2prep	no
Research prepulse	no
Diffusion mode	no
Elastography mode	no
SAR mode	high
B1 mode	default
SAR Patient data	auto
PNS mode	high
Gradient mode	default
SofTone mode	no

Hospital (2) | 20141021 CEST fMRI (13) 52:37.4 | FMRI_RESTINGSTATE 08:34.0

INFO PAGE	
Total scan duration	08:34.0
Rel. signal level (%)	100
Act. TR/TE (ms)	2000 / 25
Dyn. scan time	00:02.000
Time to k0	00:15.0
ACQ matrix M x P	96 x 95
ACQ voxel MPS (mm)	2.50 / 2.50 / 2.50
REC voxel MPS (mm)	2.50 / 2.50 / 2.50
Scan percentage (%)	100
Packages	1
Min. slice gap (mm)	0
EPI factor	37
Act. WFS (pix) / BW (Hz)	21.825 / 46.4
BW in EPI freq. dir. (Hz)	2878.9
Min. WFS (pix) / Max. BW (Hz)	21.770 / 46.5
Min. TR/TE (ms)	1999 / 12
RF avg power computed (W)	1.371604
SAR / head	< 50 %
Whole body / level	< 0.1 W/kg / normal
B1 rms	0.93 uT
PNS / level // VUIIS : dortch :	59 % / normal
Sound Pressure Level (dB)	28.01657

MOTION	
Cardiac synchronization	no
Heart rate > 250 bpm	no
Respiratory compensation	no
Navigator respiratory comp	no
Flow compensation	no
Temporal slice spacing	equidistant
fMRI echo stabilisation	no
NSA	1

DYN/ANG	
Angio / Contrast enh.	no
Quantitative flow	no
Manual start	yes
+Abuse dynamic loop	no
Dynamic study	individual
dyn scans	250
recon multiplier	1
dyn scan times	shortest
FOV time mode	default
dummy scans	5
immediate subtraction	no
fast next scan	no
synch. ext. device	yes
start at dyn.	1
interval (dyn)	119
dyn stabilization	no
prospect. motion corr.	no
Keyhole	no
Arterial Spin labeling	no

POST/PROC	
Preparation phases	full
Interactive F0	no
SENSE ref. scan	no
SmartPlan survey	no
B0 field map	no
B1 field map	no
MIP/MPR	no
Images	M, no, no, no
Autoview image	M
Calculated images	no, no, no, no
Reference tissue	Grey matter
EPI 2D phase correction	no
Preset window contrast	soft
Reconstruction mode	real time
reuse memory	no
Save raw data	no
Hardcopy protocol	no
Ringing filtering	default
Geometry correction	default

GEOMETRY	
Multi-transmit	no
Nucleus	H1
Coil selection 1	RX-Intf-1
Xmit Coil selection	MTX-Volume-T/R
User def elem sel	no
element selection	All
connection	conn-A
Coil selection 2	RX-Intf-2
element selection	All
Dual coil	yes
CLEAR	yes
body tuned	yes
FOV RL (mm)	240
AP (mm)	240
FH (mm)	115
Voxel size RL (mm)	2.5
AP (mm)	2.5
Slice thickness (mm)	2.5
Recon voxel size (mm)	2.5
Fold-over suppression	no
Reconstruction matrix	96
SENSE	yes
P reduction (AP)	2.8
P os factor	1
k-t BLAST	no
Stacks	1
type	parallel
slices	46
slice gap	user defined
gap (mm)	0
slice orientation	transverse
fold-over direction	AP
fat shift direction	P
Minimum number of packages	1
Slice scan order	default
PlanAlign	no
REST slabs	0
Catheter tracking	no
Interactive positioning	no
Allow table movement	no

OFFC/ANG	
Stacks	1
Stack Offc. AP (P=+mm)	-5.532147
RL (L=+mm)	-3.434925
FH (H=+mm)	35.45897
Ang. AP (deg)	0
RL (deg)	-5.457352
FH (deg)	0

CONTRAST	
Scan type	Imaging
Scan mode	MS
technique	FFE
+ ZOOM	no
Contrast enhancement	no
Acquisition mode	cartesian
Fast Imaging mode	EPI
shot mode	single-shot
Echoes	1
partial echo	no
shifted echo	no
TE	user defined
(ms)	25
Flip angle (deg)	63
TR	user defined
(ms)	2000
Halfscan	no
Water-fat shift	minimum
Shim	auto
mDIXON	no
Fat suppression	no
Water suppression	no
MTC	no
Research prepulse	no
Diffusion mode	no
Elastography mode	no
SAR mode	low
B1 mode	default
SAR Patient data	auto
PNS mode	low
Gradient mode	full control
max strength (mT/m)	33
max slew rate (T/m/s)	130

Hospital (2) | 20141021 CEST fMRI (13) 52:37.4 | FMRI_TRAILMAKING 04:14.0

INFO PAGE	
Total scan duration	04:14.0
Rel. signal level (%)	100
Act. TR/TE (ms)	2000 / 25
Dyn. scan time	00:02.000
Time to k0	00:15.0
ACQ matrix M x P	96 x 95
ACQ voxel MPS (mm)	2.50 / 2.50 / 2.50
REC voxel MPS (mm)	2.50 / 2.50 / 2.50
Scan percentage (%)	100
Packages	1
Min. slice gap (mm)	0
EPI factor	37
Act. WFS (pix) / BW (Hz)	21.825 / 46.4
BW in EPI freq. dir. (Hz)	2878.9
Min. WFS (pix) / Max. BW (Hz)	21.770 / 46.5
Min. TR/TE (ms)	1999 / 12
RF avg power computed (W)	1.371604
SAR / head	< 50 %
Whole body / level	< 0.1 W/kg / normal
B1 rms	0.93 uT
PNS / level // VUIIS : dortch :	59 % / normal
Sound Pressure Level (dB)	28.01657

MOTION	
Cardiac synchronization	no
Heart rate > 250 bpm	no
Respiratory compensation	no
Navigator respiratory comp	no
Flow compensation	no
Temporal slice spacing	equidistant
fMRI echo stabilisation	no
NSA	1

DYN/ANG	
Angio / Contrast enh.	no
Quantitative flow	no
Manual start	yes
+Abuse dynamic loop	no
Dynamic study	individual
dyn scans	120
recon multiplier	1
dyn scan times	shortest
FOV time mode	default
dummy scans	5
immediate subtraction	no
fast next scan	no
synch. ext. device	yes
start at dyn.	1
interval (dyn)	119
dyn stabilization	no
prospect. motion corr.	no
Keyhole	no
Arterial Spin labeling	no

POST/PROC	
Preparation phases	full
Interactive F0	no
SENSE ref. scan	no
SmartPlan survey	no
B0 field map	no
B1 field map	no
MIP/MPR	no
Images	M, no, no, no
Autoview image	M
Calculated images	no, no, no, no
Reference tissue	Grey matter
EPI 2D phase correction	no
Preset window contrast	soft
Reconstruction mode	real time
reuse memory	no
Save raw data	no
Hardcopy protocol	no
Ringing filtering	default
Geometry correction	default

GEOMETRY	
Multi-transmit	no
Nucleus	H1
Coil selection 1	RX-Intf-1
Xmit Coil selection	MTX-Volume-T/R
User def elem sel	no
element selection	All
connection	conn-A
Coil selection 2	RX-Intf-2
element selection	All
Dual coil	yes
CLEAR	yes
body tuned	yes
FOV RL (mm)	240
AP (mm)	240
FH (mm)	115
Voxel size RL (mm)	2.5
AP (mm)	2.5
Slice thickness (mm)	2.5
Recon voxel size (mm)	2.5
Fold-over suppression	no
Reconstruction matrix	96
SENSE	yes
P reduction (AP)	2.8
P os factor	1
k-t BLAST	no
Stacks	1
type	parallel
slices	46
slice gap	user defined
gap (mm)	0
slice orientation	transverse
fold-over direction	AP
fat shift direction	P
Minimum number of packages	1
Slice scan order	default
PlanAlign	no
REST slabs	0
Catheter tracking	no
Interactive positioning	no
Allow table movement	no

OFFC/ANG	
Stacks	1
Stack Offc. AP (P=+mm)	-5.532147
RL (L=+mm)	-3.434925
FH (H=+mm)	35.45897
Ang. AP (deg)	0
RL (deg)	-5.457352
FH (deg)	0

CONTRAST	
Scan type	Imaging
Scan mode	MS
technique	FFE
+ ZOOM	no
Contrast enhancement	no
Acquisition mode	cartesian
Fast Imaging mode	EPI
shot mode	single-shot
Echoes	1
partial echo	no
shifted echo	no
TE	user defined
(ms)	25
Flip angle (deg)	63
TR	user defined
(ms)	2000
Halfscan	no
Water-fat shift	minimum
Shim	auto
mDIXON	no
Fat suppression	no
Water suppression	no
MTC	no
Research prepulse	no
Diffusion mode	no
Elastography mode	no
SAR mode	low
B1 mode	default
SAR Patient data	auto
PNS mode	low
Gradient mode	full control
max strength (mT/m)	33
max slew rate (T/m/s)	130

Hospital (2) | 20141021 CEST fMRI (13) 52:37.4 | FMRI_nback 08:30.0

INFO PAGE	
Total scan duration	08:30.0
Rel. signal level (%)	100
Act. TR/TE (ms)	2500 / 25
Dyn. scan time	00:02.500
Time to k0	00:18.7
ACQ matrix M x P	96 x 95
ACQ voxel MPS (mm)	2.50 / 2.50 / 2.50
REC voxel MPS (mm)	2.50 / 2.50 / 2.50
Scan percentage (%)	100
Packages	1
Min. slice gap (mm)	0
EPI factor	37
Act. WFS (pix) / BW (Hz)	21.825 / 46.4
BW in EPI freq. dir. (Hz)	2878.9
Min. WFS (pix) / Max. BW (Hz)	21.770 / 46.5
Min. TR/TE (ms)	1999 / 12
RF avg power computed (W)	1.097284
SAR / head	< 40 %
Whole body / level	< 0.1 W/kg / normal
B1 rms	0.84 uT
PNS / level // VUIIS : dortch :	59 % / normal
Sound Pressure Level (dB)	27.13099
MOTION	
Cardiac synchronization	no
Heart rate > 250 bpm	no
Respiratory compensation	no
Navigator respiratory comp	no
Flow compensation	no
Temporal slice spacing	equidistant
fMRI echo stabilisation	no
NSA	1
DYN/ANG	
Angio / Contrast enh.	no
Quantitative flow	no
Manual start	yes
+Abuse dynamic loop	no
Dynamic study	individual
dyn scans	197
recon multiplier	1
dyn scan times	shortest
FOV time mode	default
dummy scans	5
immediate subtraction	no
fast next scan	no
synch. ext. device	yes
start at dyn.	1
interval (dyn)	119
dyn stabilization	no
prospect. motion corr.	no
Keyhole	no
Arterial Spin labeling	no
POST/PROC	
Preparation phases	full
Interactive F0	no
SENSE ref. scan	no
SmartPlan survey	no
B0 field map	no
B1 field map	no
MIP/MPR	no
Images	M, no, no, no
Autoview image	M
Calculated images	no, no, no, no
Reference tissue	Grey matter
EPI 2D phase correction	no
Preset window contrast	soft
Reconstruction mode	real time
reuse memory	no
Save raw data	no
Hardcopy protocol	no
Ringing filtering	default
Geometry correction	default

GEOMETRY	
Multi-transmit	no
Nucleus	H1
Coil selection 1	RX-Intf-1
Xmit Coil selection	MTX-Volume-T/R
User def elem sel	no
element selection	All
connection	conn-A
Coil selection 2	RX-Intf-2
element selection	All
Dual coil	yes
CLEAR	yes
body tuned	yes
FOV RL (mm)	240
AP (mm)	240
FH (mm)	115
Voxel size RL (mm)	2.5
AP (mm)	2.5
Slice thickness (mm)	2.5
Recon voxel size (mm)	2.5
Fold-over suppression	no
Reconstruction matrix	96
SENSE	yes
P reduction (AP)	2.8
P os factor	1
k-t BLAST	no
Stacks	1
type	parallel
slices	46
slice gap	user defined
gap (mm)	0
slice orientation	transverse
fold-over direction	AP
fat shift direction	P
Minimum number of packages	1
Slice scan order	default
PlanAlign	no
REST slabs	0
Catheter tracking	no
Interactive positioning	no
Allow table movement	no
OFFC/ANG	
Stacks	1
Stack Offc. AP (P=+mm)	-5.532147
RL (L=+mm)	-3.434925
FH (H=+mm)	35.45897
Ang. AP (deg)	0
RL (deg)	-5.457352
FH (deg)	0

CONTRAST	
Scan type	Imaging
Scan mode	MS
technique	FFE
+ ZOOM	no
Contrast enhancement	no
Acquisition mode	cartesian
Fast Imaging mode	EPI
shot mode	single-shot
Echoes	1
partial echo	no
shifted echo	no
TE	user defined
(ms)	25
Flip angle (deg)	63
TR	user defined
(ms)	2500
Halfscan	no
Water-fat shift	minimum
Shim	auto
mDIXON	no
Fat suppression	no
Water suppression	no
MTC	no
Research prepulse	no
Diffusion mode	no
Elastography mode	no
SAR mode	low
B1 mode	default
SAR Patient data	auto
PNS mode	low
Gradient mode	full control
max strength (mT/m)	33
max slew rate (T/m/s)	130

Hospital (2) | 20141021 CEST fMRI (13) 52:37.4 | T1_3D_TFE_quantGeo 00:55.7

INFO PAGE	
Total scan duration	00:55.7
Rel. signal level (%)	100
Act. TR/TE (ms)	2.8 / 1.44
ACQ matrix M x P	192 x 190
ACQ voxel MPS (mm)	1.25 / 1.26 / 2.50
REC voxel MPS (mm)	0.94 / 0.94 / 2.50
Scan percentage (%)	98.9899
TFE shots	13
TFE dur. shot / acq (ms)	1675.7 / 729.0
Min. TI delay	386.7124
Act. WFS (pix) / BW (Hz)	0.778 / 1302.1
Min. WFS (pix) / Max. BW (Hz)	0.774 / 1308.4
RF avg power computed (W)	0.8993402
SAR / head	< 33 %
Whole body / level	0.0 W/kg / normal
B1 rms	0.76 uT
PNS / level // VUIIS : dortch :	59 % / normal
Sound Pressure Level (dB)	29.78219
MOTION	
Cardiac synchronization	no
Heart rate > 250 bpm	no
Respiratory compensation	no
Navigator respiratory comp	no
Flow compensation	no
fMRI echo stabilisation	no
Motion smoothing	no
NSA	1
DYN/ANG	
Angio / Contrast enh.	no
Quantitative flow	no
CENTRA	no
Manual start	no
+Abuse dynamic loop	no
Dynamic study	no
Arterial Spin labeling	no
POST/PROC	
Preparation phases	auto
Interactive F0	no
SENSE ref. scan	no
SmartPlan survey	no
B0 field map	no
B1 field map	no
MIP/MPR	no
Images	M, no, no, no
Autoview image	M
Calculated images	no, no, no, no
Reference tissue	Grey matter
Preset window contrast	soft
Reconstruction mode	immediate
Save raw data	no
Hardcopy protocol	no
Ringing filtering	rectangular
Geometry correction	default
Elliptical k-space shutter	default

GEOMETRY	
Multi-transmit	no
Nucleus	H1
Coil selection 1	RX-Intf-1
Xmit Coil selection	MTX-Volume-T/R
User def elem sel	no
element selection	All
connection	conn-A
Coil selection 2	RX-Intf-2
element selection	All
Dual coil	yes
CLEAR	yes
body tuned	yes
FOV RL (mm)	240
AP (mm)	240
FH (mm)	165
Voxel size RL (mm)	1.25
AP (mm)	1.254902
FH (mm)	2.5
Recon voxel size (mm)	0.94
Fold-over suppression	no
Slice oversampling	default
RF select. FOS	no
Reconstruction matrix	256
SENSE	yes
P reduction (AP)	2
P os factor	1
S reduction (FH)	2
k-t BLAST	no
Overcontiguous slices	no
Stacks	1
slices	66
slice orientation	transverse
fold-over direction	AP
fat shift direction	L
Chunks	1
PlanAlign	no
REST slabs	0
Catheter tracking	no
Interactive positioning	no
Allow table movement	no
OFFC/ANG	
Stacks	1
Stack Offc. AP (P=+mm)	-4.247866
RL (L=+mm)	-3.434925
FH (H=+mm)	35.88707
Ang. AP (deg)	0
RL (deg)	-5.457352
FH (deg)	0

CONTRAST	
Scan type	Imaging
Scan mode	3D
technique	FFE
+ ZOOM	no
Contrast enhancement	T1
Acquisition mode	cartesian
Fast Imaging mode	TFE
3D non-selective	no
shot mode	multishot
TFE factor	256
3D free factor	no
startup echoes	default
+TFE followup echoes	0
shot interval	user defined
(ms)	4500
profile order	linear
turbo direction	radial
CENTRA (spiral)	no
Echoes	1
partial echo	no
shifted echo	no
TE	shortest
Flip angle (deg)	7
TR	shortest
Halfscan	no
Water-fat shift	minimum
Shim	auto
mDIXON	no
Fat suppression	no
Water suppression	no
TFE prepulse	invert
slice selection	no
delay	user defined
(ms)	1300
PSIR	no
+inv pulse type	+B1 opt (low BW)
MTC	no
T2prep	no
Research prepulse	no
Diffusion mode	no
Elastography mode	no
SAR mode	high
B1 mode	default
SAR Patient data	auto
PNS mode	low
Gradient mode	full control
max strength (mT/m)	33
max slew rate (T/m/s)	166

Hospital (2) | 20141021 CEST fMRI (13) 52:37.4 | T2star_multiEcho 01:02.7

INFO PAGE	
Total scan duration	01:02.7
Rel. signal level (%)	100
Act. TR/TE1/delta TE (ms)	34 / 3.3 / 3.2
ACQ matrix M x P	240 x 240
ACQ voxel MPS (mm)	1.00 / 1.00 / 5.00
REC voxel MPS (mm)	0.94 / 0.94 / 5.00
Scan percentage (%)	100
Act. WFS (pix) / BW (Hz)	1.418 / 714.8
Min. WFS (pix) / Max. BW (Hz)	1.125 / 900.9
RF avg power computed (W)	0.1353424
SAR / head	< 5 %
Whole body / level	0.0 W/kg / normal
B1 rms	0.29 uT
PNS / level // VUIIS : dortch :	60 % / normal
Sound Pressure Level (dB)	29.7646

MOTION	
Cardiac synchronization	no
Heart rate > 250 bpm	no
Respiratory compensation	no
Navigator respiratory comp	no
Flow compensation	yes
fMRI echo stabilisation	no
NSA	1

DYN/ANG	
Angio / Contrast enh.	inflow
Quantitative flow	no
Tone pulse	no
Manual start	no
+Abuse dynamic loop	no
Dynamic study	no
Arterial Spin labeling	no

POST/PROC	
Preparation phases	auto
Interactive F0	no
SENSE ref. scan	no
SmartPlan survey	no
B0 field map	no
B1 field map	no
MIP/MPR	no
Images	M, R, I, no
Autoview image	M
Calculated images	T2, no, no, no
T2* clipvalue (ms)	100
Reference tissue	Grey matter
Preset window contrast	soft
Reconstruction mode	immediate
Save raw data	no
Hardcopy protocol	no
Ringing filtering	default
Geometry correction	default
Elliptical k-space shutter	no

GEOMETRY	
Multi-transmit	no
Nucleus	H1
Coil selection 1	RX-Intf-1
Xmit Coil selection	MTX-Volume-T/R
User def elem sel	no
element selection	All
connection	conn-A
Coil selection 2	RX-Intf-2
element selection	All
Dual coil	yes
CLEAR	yes
body tuned	yes
FOV AP (mm)	240
RL (mm)	240
FH (mm)	60
Voxel size AP (mm)	1
RL (mm)	1
FH (mm)	5
Recon voxel size (mm)	0.9375
Fold-over suppression	no
Slice oversampling	default
RF select. FOS	no
Reconstruction matrix	256
SENSE	yes
P reduction (RL)	2
P os factor	1
S reduction (FH)	1
k-t BLAST	no
Overcontiguous slices	no
Stacks	1
slices	12
slice orientation	transverse
fold-over direction	RL
fat shift direction	P
Chunks	1
PlanAlign	no
REST slabs	0
Catheter tracking	no
Interactive positioning	no
Allow table movement	no

OFFC/ANG	
Stacks	1
Stack Offc. AP (P=+mm)	-5.532147
RL (L=+mm)	-3.434925
FH (H=+mm)	35.45897
Ang. AP (deg)	0
RL (deg)	-5.457352
FH (deg)	0
Shim Size AP (mm)	180.7495
RL (mm)	134.1432
FH (mm)	114.2866
Offc. AP (P=+mm)	-1.87074
RL (L=+mm)	-3.660397
FH (H=+mm)	33.86363
Ang. AP (deg)	2.26406
RL (deg)	-6.580403
FH (deg)	4.637685

CONTRAST	
Scan type	Imaging
Scan mode	3D
technique	FFE
loop order	zy_order
+ ZOOM	no
Contrast enhancement	T1
Acquisition mode	cartesian
Fast Imaging mode	none
3D non-selective	no
Echoes	10
partial echo	no
shifted echo	no
TE first	shortest
echospacing	shortest
flyback	yes
Flip angle (deg)	8
TR	shortest
Halfscan	no
Water-fat shift	user defined
(pixels)	1.4
Shim	PB-volume
ShimAlign	no
mDIXON	no
Fat suppression	no
Water suppression	no
MTC	no
Research prepulse	no
Diffusion mode	no
Elastography mode	no
SAR mode	low
B1 mode	default
SAR Patient data	auto
PNS mode	low
Gradient mode	maximum
SofTone mode	no

Appendix 2

Exam Card

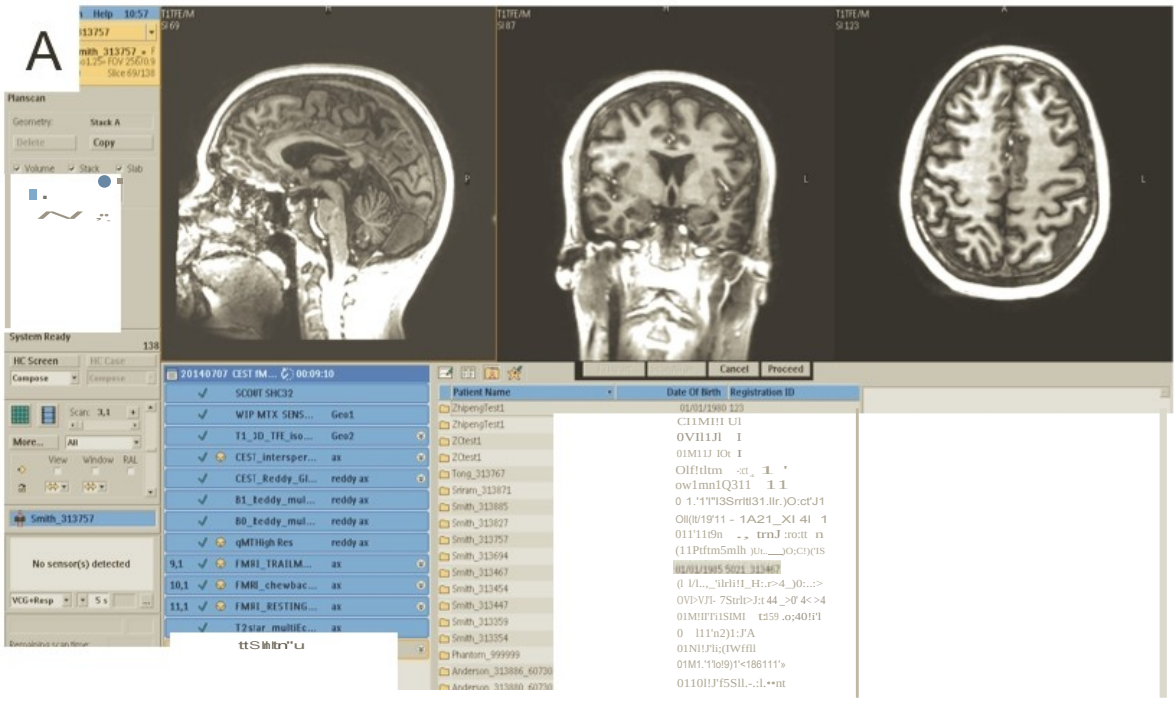

Viewing Environment

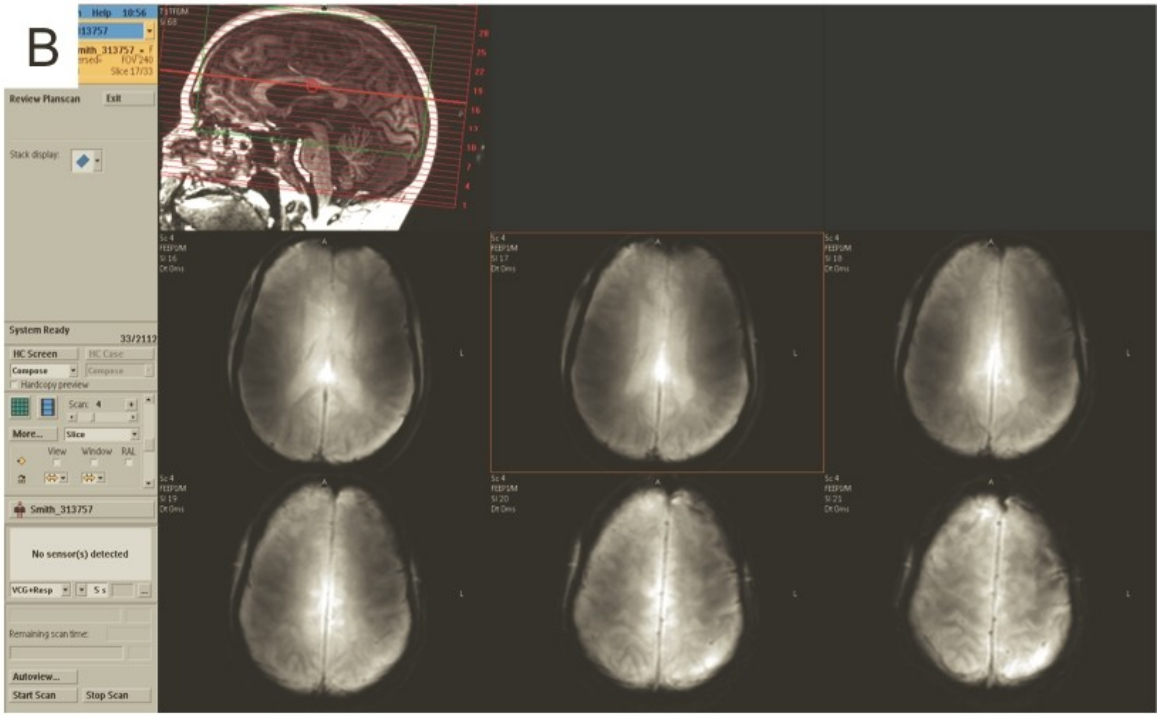

Appendix 3

NeuroImage 64 (2013) 640–649

Contents lists available at SciVerse ScienceDirect

NeuroImage

journal homepage: www.elsevier.com/locate/ynimg

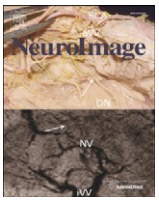

Quantitative magnetization transfer imaging of human brain at 7 T

Richard D. Dortch [a,b,*], Jay Moore [a,b], Ke Li [a,b], Marcin Jankiewicz [a,b], Daniel F. Gochberg [a,b,c], Jane A. Hirtle [b], John C. Gore [a,b,c,d,e], Seth A. Smith [a,b,d]

[a] Department of Radiology and Radiological Sciences, Vanderbilt University, Nashville, TN, USA
[b] Vanderbilt University Institute of Imaging Science, Vanderbilt University, Nashville, TN, USA
[c] Department of Physics and Astronomy, Vanderbilt University, Nashville, TN, USA
[d] Department of Biomedical Engineering, Vanderbilt University, Nashville, TN, USA
[e] Department of Molecular Physiology and Biophysics, Vanderbilt University, Nashville, TN, USA

article info

Article history:
Accepted 18 August 2012
Available online 23 August 2012

Keywords:
Magnetization transfer
7 T
White matter
Myelin
Brain
Multiple sclerosis

abstract

Quantitative magnetization transfer (qMT) imaging yields indices describing the interactions between free water protons and immobile macromolecular protons. These indices include the macromolecular to free pool size ratio (PSR), which has been shown to be correlated with myelin content in white matter. Because of the long scan times required for whole-brain imaging (≈ 20–30 min), qMT studies of the human brain have not found widespread application. Herein, we investigated whether the increased signal-to-noise ratio available at 7.0 T could be used to reduce qMT scan times. More specifically, we developed a selective inversion recovery (SIR) qMT imaging protocol with a i) novel transmit radiofrequency (B_1^+) and static field (B_0) insensitive inversion pulse, ii) turbo field-echo readout, and iii) reduced TR. In vivo qMT data were obtained in the brains of healthy volunteers at 7.0 T using the resulting protocol (scan time ≈ 40 s/slice, resolution = 2 × 2 × 3 mm^3). Reliability was also assessed in repeated acquisitions. The results of this study demonstrate that SIR qMT imaging can be reliably performed within the radiofrequency power restrictions present at 7.0 T, even in the presence of large B_1^+ and B_0 inhomogeneities. Consistent with qMT studies at lower field strengths, the observed PSR values were higher in white matter (mean ± SD = 17.6 ± 1.3%) relative to gray matter (10.3 ± 1.6%) at 7.0 T. In addition, regional variations in PSR were observed in white matter. Together, these results suggest that qMT measurements are feasible at 7.0 T and may eventually allow for the high-resolution assessment of changes in composition throughout the normal and diseased human brain in vivo.

Introduction

In addition to the free water protons typically observed in magnetic resonance imaging (MRI), there are protons residing on immobile macromolecules in tissue (Wolff and Balaban, 1989). Typical imaging sequences do not directly detect this pool of protons because they exhibit very short transverse relaxation times (≈ 10 μs) and, therefore, lose coherence before their signal can be captured. This macromolecule proton pool can, however, be indirectly detected by exploiting its interactions with the free water pool via chemical exchange and/or dipolar mechanisms [referred to together as the magnetization transfer (MT) effect]. Previous phantom studies (Koenig, 1991; Kucharczyk et al., 1994) have shown that the bulk of the MT effect in white matter (WM) arises from myelin-associated lipids, which suggests that MT contrast may be a more specific marker for myelin pathology than conventional imaging methods. As a result, there is considerable interest in exploiting MT contrast to assay changes in myelination associated with a number of diseases [e.g., multiple sclerosis (Catalaa et al., 2000; Filippi and Rocca, 2004; Gass et al., 1994; Kalkers et al., 2001) and neuropsychiatric diseases (Bruno et al., 2004; Kabani et al., 2002a, 2002b)].

MT contrast can be generated by applying an off-resonance radiofrequency (RF) prepulse to selectively saturate the spectrally broad macromolecular proton pool (Wolff and Balaban, 1989). This saturation then transfers to the free water proton pool via MT, resulting in a decrease in the observed free water signal. The magnitude of this effect can be characterized by a semi-quantitative metric known as the magnetization transfer ratio (Dousset et al., 1992): $MTR = 1 - S_{sat}/S_0$, where S_{sat} and S_0 are the observed signal intensities with and without the application of an MT saturation prepulse, respectively. Although the MTR has been shown to correlate with myelin content (Odrobina et al., 2005; Schmierer et al., 2004), it is also sensitive to the choice of experimental parameters such as RF power (Berry et al., 1999) as well as non-MT-specific NMR parameters such as tissue relaxation times (Henkelman et al., 1993). As a result, quantitative MT (qMT) approaches have been developed. These qMT approaches

Grant sponsors: NIH K01 EB009120 (SAS), NIH T32 EB001628 (JCG), NIH EB00461 (JCG), and Vanderbilt Bridge Funding (DFG).

* Corresponding author at: Vanderbilt University Institute of Imaging Science, AA-1101 Medical Center North, 1161 21st Avenue South, Nashville, TN 37232-2310, USA. Fax: +1 615 322 0734.
E-mail address: richard.dortch@vanderbilt.edu (R.D. Dortch).

1053-8119/$ – see front matter © 2012 Elsevier Inc. All rights reserved.
http://dx.doi.org/10.1016/j.neuroimage.2012.08.047

quantify distinct tissue characteristics (e.g., the size of the macromolecular pool, rate of MT exchange) rather than the combined effect of multiple tissue and/or acquisition parameters. As such, qMT measures are thought to yield more specific information on tissue composition than the MTR.

Pulsed saturation qMT imaging (Graham and Henkelman, 1997; Pike, 1996; Sled and Pike, 2000, 2001) has received considerable attention for application in humans in vivo because it allows for the rapid collection of qMT data within the hardware constraints of most clinical systems. This approach involves a steady-state, spoiled gradient-echo acquisition interleaved with an MT-preparation pulse. By collecting images over a range of MT pulse offset frequencies and/or powers and fitting the resulting data to a two-pool model of the MT effect, one can extract parameters such as the macromolecular to free pool size ratio (PSR) and the rate of MT exchange. Previous work has shown that the PSR is correlated with myelin content (Odrobina et al., 2005; Ou et al., 2009; Schmierer et al., 2007; Underhill et al., 2011). The relationship between the rate of MT exchange and underlying tissue composition is less clear; however, previous work has suggested that the rate of MT exchange may reflect changes within the myelin lipid structure (Smith et al., 2009).

Unfortunately, qMT imaging has not found widespread application in practice. This can be attributed in part to the long scan times (≈ 20–30 min for whole-brain imaging) required to collect images at multiple offset frequencies and/or powers. The number of total images required can be reduced by designing optimal sampling strategies (Cercignani and Alexander, 2006; Levesque et al., 2011) or by fixing certain model parameters in the fitting procedure (Underhill et al., 2009, 2011). Potentially more efficient strategies based upon steady-state free-precession (SSFP) sequences (Garcia et al., 2010; Gloor et al., 2008) may also be employed.

As an alternative, or perhaps in combination with these strategies, one could translate qMT imaging approaches to higher field strengths. The resulting increase in SNR could then be used to obtain more reliable estimates of MT parameters or traded to reduce scan times and/or increase resolution. To date, qMT studies in humans in vivo have been primarily limited to 1.5 and 3.0 T and we are aware of only one report (Mougin et al., 2010) of MT parameters in the human brain in vivo at 7.0 T. The translation of pulsed saturation approaches to 7.0 T faces two primary challenges: i) RF power limitations [e.g., specific absorption ratio (SAR) limitations] and ii) transmit RF (B_1^+) and static magnetic field (B_0) inhomogeneities. SSFP-based approaches may also be limited at high field by banding artifacts associated with B_0 inhomogeneities. In contrast, selective inversion recovery (SIR) qMT imaging (Edzes and Samulski, 1977; Gochberg et al., 1997), which is based upon measuring the biexponential recovery of the free water pool in the presence of MT after an on-resonance inversion pulse, has been suggested (Dortch et al., 2011) to be less sensitive to these issues. Note that this approach is similar to the stimulated echo approach proposed by Ropele et al. (2003); therefore, both approaches may be well suited for qMT imaging at 7.0 T.

In this study, we have investigated the feasibility of using the SIR approach for high field qMT imaging of the human brain. More specifically, we have translated our previously published 3.0-T SIR protocol (Dortch et al., 2011) to 7.0 T with two significant modifications. First, we incorporated a novel B_1^+- and $!1B_0$-insensitive composite inversion pulse to ensure a more uniform inversion of the free water pool over the whole brain. Second, we transitioned from a turbo-spin echo readout (TSE) to a turbo field-echo readout (TFE)—similar to an MP-RAGE sequence (Mugler and Brookeman, 1990)—as the former is susceptible to B_1^+-related artifacts (due to imperfect refocusing) and is SAR-limited at high field. The TFE readout has the added benefit of covering k-space more efficiently than the TSE readout, which, in combination with some additional protocol optimization, allowed us to transition from a single-slice approach at 3.0 T to a whole-brain approach at 7.0 T (≈ 40 s/slice at 2.0 × 2.0 × 3.0 mm^3 resolution). Using this protocol, in vivo qMT data were obtained in the brains of 13 healthy volunteers at 7.0 T. To assess the reproducibility of the technique, six of the healthy volunteers were scanned twice. Additional numerical simulations were performed to determine the effect of TFE readout on our qMT parameter maps.

Theory

Consider free water (f) and macromolecular (m) proton pools between which MT can occur. Define unique equilibrium magnetizations (M_{0f} and M_{0m}), spin–lattice relaxation rates (R_{1f} and R_{1m}), and spin–spin relaxation rates (R_{2f} and R_{2m}) for each pool as well as an MT rate from the macromolecular to the free pool (k_{mf})—the rate in the other direction can be determined from $k_{fm} = k_{mf}M_{0m}/M_{0f}$. Assume MT of transverse magnetization to be negligible because of the short T_2 of the macromolecular pool. In this case, the transverse components of the macromolecular pool can be ignored. The time evolution of the remaining x, y, and z components of the magnetization vector $M = [M_{xf}\ M_{yf}\ M_{zf}\ M_{zm}]^T$ during a constant amplitude RF pulse can be expressed in matrix form as (Portnoy and Stanisz, 2007)

$$\frac{dM(t)}{dt} = AM(t) + B; \quad (1)$$

where

$$A = \begin{bmatrix} -R_{2f} & \omega & -\omega_1 \sin\phi & 0 \\ -\omega & -R_{2f} & \omega_1 \cos\phi & 0 \\ \omega_1 \sin\phi & -\omega_1 \cos\phi & -R_{1f} + k_{fm} & k_{mf} \\ 0 & 0 & k_{fm} & -R_{1m} + R_{RF} + k_{mf} \end{bmatrix}, \quad (2)$$

$$B = \begin{bmatrix} 0 \\ 0 \\ R_{1f}M_{0f} \\ R_{1m}M_{0m} \end{bmatrix};$$

ω is the frequency offset from resonance for the RF pulse, ω_1 is the frequency of precession about the RF pulse, and ϕ is the phase of the RF pulse in the transverse plane. The standard Bloch equations implicitly assume a Lorentzian lineshape, which is invalid for the macromolecular proton pool. As a result, the Bloch equations for the macromolecular pool have been replaced in Eq. (2) by a single longitudinal component whose saturation is governed by the rate $R_{RF} = \pi\omega_1^2 g_m(\omega)$, where g_m is the lineshape function of the macromolecular pool. When applying off-resonance irradiation, a super-Lorentzian lineshape is typically used to model biological macromolecular protons (Morrison et al., 1995). Because the super-Lorentzian exhibits an on-resonance singularity, Gaussian (Gochberg and Gore, 2007) or super-Lorentzian functions extrapolated from a 1 kHz offset (Gloor et al., 2008) are typically used to model the macromolecular pool lineshape pool during on-resonance irradiation.

The general solution to this system of equations can be expressed as

$$M(t) = \exp(At)M(0) + [\exp(At) - I]A^{-1}B; \quad (3)$$

where M(0) is the initial condition of the system and I is an identity matrix. The same expression can be used to describe the system during free precession (i.e., when $\omega_1 = 0$). In this case, the solution can be further simplified by noting that the z-component is decoupled from the x- and y-components, resulting in the following expression for the longitudinal magnetization vector $M_z = [M_{zf}\ M_{zm}]^T$

$$M_z(t) = \exp(A_z t)M(0) + [I - \exp(A_z t)]M_0; \quad (4)$$

where $M_0 = [M_{0f}\ M_{0m}]^T$ and A_z is the lower-right quadrant of A with $R_{RF} = 0$. Expanding the matrix exponentials in this expression yields

$$M_z(t_i) = \begin{bmatrix} e^{-\lambda^+ t_i} & 0 \\ 0 & e^{-\lambda^- t_i} \end{bmatrix} U \begin{bmatrix} M_{0f} \\ 0 \end{bmatrix} + \begin{bmatrix} 0 \\ e^{-\lambda^- t_i} \end{bmatrix} U^{-1} \begin{bmatrix} M_{0f} \\ M_{0m} \end{bmatrix}; \quad (5)$$

where $\lambda^{+/-}$ are the negative eigenvalues of A_z and U is a matrix whose columns are the corresponding eigenvectors. From Eq. (5), it can be seen that M_{zf} recovers as a biexponential function governed by the fast and slow rate constants λ^+ and λ^-, respectively, during free precession. As described below, one can obtain estimates of qMT parameters (e.g., PSR and k_{mf}) by measuring this biexponential recovery.

Methods

Pulse sequence

The SIR qMT sequence (Fig. 1) used herein is similar to the inversion recovery sequence used to measure T_1 with two modifications. First, short inversion times ($\approx$ 10 ms or less) are sampled in order to capture the fast-recovering λ^+ component of the biexponential recovery. Second, a T_2-selective inversion pulse is applied. This is achieved via a low power inversion pulse whose duration is much longer than the T_2 of the macromolecular pool ($T_{2m} \approx 10$ μs) and much shorter than the T_2 of the free water pool ($T_{2f} \approx$ 10–100 ms). Ideally, this pulse inverts M_{zf} with minimal saturation of M_{zm}. In other words, this pulse maximizes the difference between the pools and, in turn, the sensitivity of the signal to MT. This is followed by a variable duration inversion recovery period to sample the transient biexponential recovery of M_{zf} and a center-out TFE readout (SIR-TFE) to efficiently sample k-space. For inversion recovery acquisitions, a predelay time $t_d \approx 5/\lambda^-$ is commonly employed to ensure full recovery of M_{zf}. However, if one can assume that the longitudinal magnetization of both pools is approximately zero at the end of the readout, the effect of a shorter predelay period can be accounted for in the signal model, allowing one to reduce t_d (and scan times) without biasing the estimated parameters. This assumption has been previously shown to hold true for a TSE readout (Gochberg and Gore, 2007); however, this cannot be assumed for the TFE readout employed herein. As a result, we empirically designed a train of RF pulses [number of pulses = 32, $\alpha = 135°$, pulse spacing = 20 ms, pulse train duration (t_{sat}) = 620 ms] to saturate both pools following the TFE readout. To assess the effect of this pulse train on the longitudinal magnetization of both pools, numerical simulations were performed via Eq. (3) and the following parameters: $R_{1m} = R_{1f} = 0.8\ s^{-1}$, $T_{2m} = 10$ μs (Gaussian lineshape), $T_{2f} = 60$ ms, $k_{mf} = 15\ s^{-1}$, and PSR = 15%. The results from these simulations indicate that this pulse train saturates both pools [$M_{zf}(t_{sat})/M_{0f} \leq 0.01$ and $M_{zm}(t_{sat})/M_{0m} \leq 0.06$] over the range of expected B_1^+ values ($B_{1,actual}^+/B_{1,nominal}^+ = 0.3$–$1.0$) in the human brain at 7.0 T [n.b., the manufacturer-provided power optimization tended to yield a mean $B_{1,actual}^+/B_{1,nominal}^+ \geq 1.0$ (Moore et al., 2010)].

Plugging the initial condition of $M_z(t_d = 0) = 0$ into Eq. (4), signal equations can be generated for the predelay period of the SIR-TFE sequence. The ending values for this period can then be used as the initial condition for the inversion recovery period, taking account for the effect of the inversion pulse

$$M_z(t^+) = SM_z(t^-); \quad (6)$$

where S is a diagonal matrix with elements that account for the inversion of the free pool ($S_f = -1$ denotes complete inversion) and the saturation of the macromolecular pool ($S_m = 1$ denotes no saturation) and $t^{+/-}$ is the time immediately before/after the pulse. This yields the final expression for the evolution of M_z during the SIR period of the sequence

$$M_z(t_i; t_d) = [\exp(A_z t_i) S][I - \exp(A_z t_d)] + [I - \exp(A_z t_i)] M_0. \quad (7)$$

In addition to these pulse sequence modifications, a novel 64-element composite inversion pulse was designed and employed herein to ensure a uniform inversion of M_{zf} over the range of B_1^+ and ΔB_0 values previously measured in the human brain at 7.0 T (Moore et al., 2010). The optimization procedure (Moore et al., 2010) tended to produce high power pulses with suboptimal T_2-selectivity. As a result, we included an additional RF power constraint into the procedure, which was weighted against the uniform inversion constraint. The resulting amplitudes and phases of the subpulses are shown in Fig. 2. To evaluate the pulse's performance, S_f and S_m were estimated from Eq. (6) by propagating Eq. (3) through each of the 64 subpulses [neglecting T_1 relaxation and MT during the pulse and

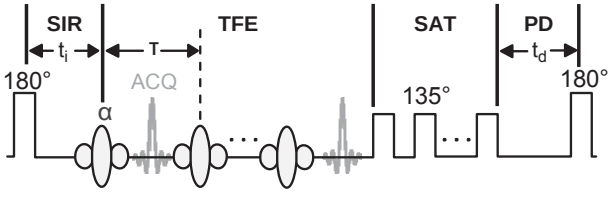

Fig. 1. SIR-TFE pulse sequence diagram. The sequence employs i) a composite inversion pulse (Fig. 2) designed to uniformly invert M_{zf} over a range of expected ΔB_0 and B_1^+ values with minimal macromolecular pool saturation, ii) a variable duration inversion recovery (SIR) period to sample the free pool recovery, iii) a TFE readout to efficiently cover k-space, iv) a pulse train to saturate (SAT) the free and macromolecular pools (allows $t_d \geq 5/\lambda^-$), and v) a predelay (PD) period to allow for partial M_z recovery. Legend: t_i = inversion time, t_d = predelay, τ = TFE pulse-to-pulse interval, ACQ = acquisition.

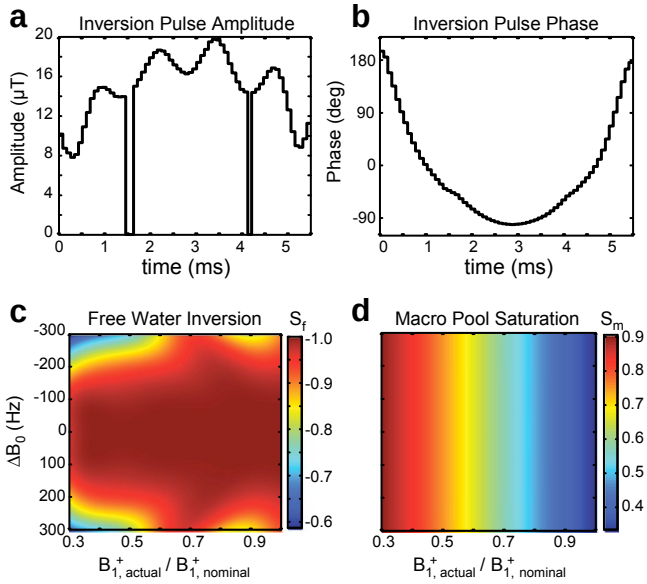

Fig. 2. Composite inversion pulse amplitudes (a), phases (b), predicted free water inversion efficiency S_f (c), and predicted macromolecular saturation fractions S_m (d). $S_f = -1$ denotes complete inversion; $S_m = 1$ denotes no saturation. The two zero-amplitude discontinuities in the RF pulse (a) are a consequence of the power constraint used in the minimization procedure. The RF phase (b) of the pulse at these discontinuities is arbitrary; therefore, the phase at these points was set based upon linear interpolation of the neighboring RF phases for display purposes.

assuming a Gaussian macromolecular pool lineshape with $T_{2m} = 10$ μs (Gochberg and Gore, 2007)]. From this procedure, the pulse is predicted to yield a uniform inversion of M_{zf} over a wide range of B_1^+ and ΔB_0 values without complete saturation of M_{zm}.

Numerical simulations

The TFE readout employed herein effectively blurs the image along the phase-encoding direction according to its readout point-spread function (PSF), which is a complex function of the sequence timings and the NMR parameters of the tissue (Constable and Gore, 1992). If the readout PSF is constant as a function of t_i, then its effect will be to simply blur the final MT parameter maps. If, however, the readout PSF changes as a function of t_i, each image will be blurred to a different degree, potentially biasing the final parameter maps.

To evaluate this effect, the SIR-TFE signal arising from a one-dimensional (1D) test object was numerically simulated. As shown in Fig. 3, MT parameters were defined for test object regions representing white matter (WM), gray matter (GM), and cerebrospinal fluid (CSF). For each region and t_i, the signal evolution during each RF pulse and precession period of the TFE readout was simulated from Eq. (3) with the imaging parameters in the Data acquisition section—using $M_z(t_i)$ from Eq. (7) as the initial condition and replacing each time-varying excitation pulse with a constant amplitude pulse of equivalent flip angle or root-mean-squared power (Ramani et al., 2002) for the free water or macromolecular pool, respectively. Complete spoiling of transverse magnetization was assumed prior to each RF pulse. The resulting M_{zf} immediately after each RF pulse was taken to represent the signal as a function of echo number. The signal was then re-ordered to account for the k-space trajectory and SENSE acceleration used, and the resulting re-ordered signal was taken to represent a k-space filter. To apply the k-space filters to the 1D test object, each uniform object region was Fourier transformed into k-space, multiplied by its corresponding k-space filter, and inverse Fourier transformed back into image space. The resulting object regions were then summed to generate the final blurred 1D object at each t_i. Finally, to assess the effect of the TFE readout on qMT parameter maps, the magnitude of the blurred test object signal at each voxel was fit to the M_{zf} component of Eq. (7) as described in the Data analysis section.

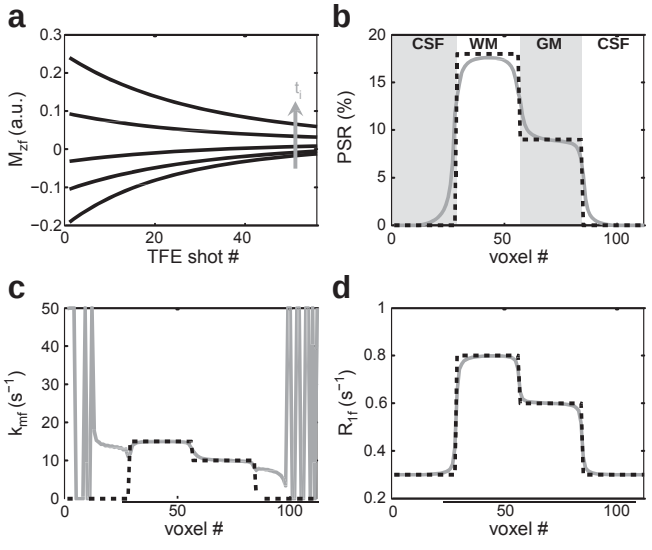

Fig. 3. Numerical simulations of the SIR-TFE readout (a) and resulting qMT parameter fits for the 1D test object defined in (b–d). (a) The M_{zf} for each region (WM shown here) and t_i was simulated and reordered into the corresponding k-space filter. The resulting filters were applied to the 1D test object as described in the text. (b–d) From the simulated fit parameters (solid gray lines), it can be seen that the TFE readout blurs the parameter maps with little or no bias (except for k_{mf} in CSF regions, which do not exhibit an MT effect).

Subjects

MRI was performed on thirteen healthy volunteers (22–37 years old, 10 male, 3 female). To test reproducibility, six of the healthy volunteers were asked to undergo a second MRI scan at least two weeks after the first session. The study was approved by our local institutional review board, and signed consent was obtained prior to all examinations.

Data acquisition

Imaging was performed using a 7.0-T, Philips Achieva MR scanner (Philips Healthcare, Best, The Netherlands). A quadrature volume coil was used for excitation and a 32-channel head coil (Nova Medical, Wilmington, MA, USA) was used for signal reception. For qMT imaging, SIR-TFE data were collected in each subject using the general pulse sequence shown in Fig. 1.

An initial experiment was performed in one healthy volunteer to determine the effect of the post-TFE saturation train and predelay time t_d on the qMT parameter maps. For this initial experiment, SIR-TFE data were acquired in a single 5-mm axial slice with and without the post-TFE saturation train (see Fig. 1, shaded area labeled SAT) over a range of t_d values (0.125–10 s). Additional imaging parameters included: t_i logarithmically spaced between 6 ms and 2 s (15 values) and t_i = 10 s, TFE echoes per shot = 53, TFE pulse-to-pulse interval (τ)/TE/α = 2.8 ms/1.4 ms/15°, SENSE factor = 2, field-of-view = 212 × 212 mm^2, resolution = 2.0 × 2.0 mm^2, and number of signal acquisitions averaged (NSA) = 2.

Based upon the results of this experiment along with previous numerical simulations (Gochberg and Gore, 2007), a t_d of 2.5 s was chosen to balance the scan time and SNR constraints for whole-brain SIR-TFE imaging. Whole-brain qMT data were acquired in 12 volunteers (six scanned twice) via a three-dimensional (3D) SIR-TFE sequence using the previously listed parameters except: t_i logarithmically spaced between 6 ms and 2 s (13 values) and t_i = 8 s, SENSE factor = 4 (2 anterior–posterior, 2 superior–inferior), field-of-view = 212 × 212 × 90 mm^3, resolution = 2.0 × 2.0 × 3.0 mm^3, and NSA = 1. This resulted in an acquisition time ≈ 19 min for 30 slices.

Recall that the signal model [Eq. (7)] has terms (S_f and S_m) that account for the effect of the inversion pulse on the free and macromolecular pool magnetizations. S_f was included as a free parameter in the fit as described in the Data analysis section, while S_m was numerically estimated as described in the Pulse sequence section. Because S_m is sensitive to B_1^+ (see Fig. 2d), this numerical estimation required an independent measurement of B_1^+. As a result, B_1^+ was estimated in same volume as the SIR-TFE data using the actual flip angle imaging (AFI) method (Yarnykh, 2007) with TR_1/TR_2 = 125/25 ms and a 60° slab-selective excitation pulse (asymmetric sinc pulse with Gaussian apodization).

Data analysis

All data analyses were performed in MATLAB (Mathworks, Natick, MA). Prior to data fitting, each SIR-TFE and AFI volume was co-registered to the SIR-TFE volume acquired at t_i = 110 ms (middle value) using a 3D rigid body registration based upon normalized mutual information (Viola and Wells, 1997). Following co-registration, automatic brain extraction was performed (Smith, 2002) and qMT parameter maps were calculated in each volunteer. The SIR-TFE signal model described in Eq. (7) has seven independent parameters: R_{1m}, R_{1f}, S_m, S_f, M_{0f}, PSR = M_{0m}/M_{0f}, and k_{mf} ($k_{fm} = k_{mf}$PSR). As is the

case with pulsed saturation methods, the signal dependence on R_{1m} for SIR data is weak (Li et al., 2010). Therefore, R_{1m} was set equal to R_{1f} for fitting purposes. The parameter S_m was numerically estimated for each voxel. This required an independent estimate of the actual flip angle in each voxel (α_{actual}), which was calculated from the AFI data using the following relationship (Yarnykh, 2007):

$$\alpha_{actual} = \cos^{-1}\left(\frac{rn-1}{n-r}\right); \quad (8)$$

where $n = TR_2/TR_1$, $r = S(TR_2)/S(TR_2)$, and S is the signal intensity. The resulting α_{actual} map was smoothed with a $10 \times 10 \times 9$ mm^3 moving-average filter to minimize the impact of imaging artifacts. Following this operation, the flip angle values were converted to $B^{+}_{1,actual}$ values for the composite inversion pulse (see Fig. 2a) and S_m was estimated using the procedure described in the Pulse sequence section (see Fig. 2d). The remaining five parameters (R_{1f}, S_f, M_{0f}, k_{mf}, and PSR) were estimated for each voxel by fitting SIR-TFE data (14 t_i values) to the M_{zf} component of Eq. (7) in a least-squares sense using the procedure described in Dortch et al. (2011).

SIR-TFE data had a mean SNR per voxel of 180 ± 50 (range = 60–320) within the defined ROIs, where SNR is defined as M_{0f} divided by the standard deviation (SD) of the residuals of the fit. Monte Carlo simulations, similar to those described by Li et al. (2010), were performed to predict the uncertainty of the fit parameters at these SNR levels. The t_i and t_d values listed above were used for these simulations. Additional simulation parameters included: $R_{1m} = R_{1f} = 0.8\ s^{-1}$, $k_{mf} = 15\ s^{-1}$, PSR = 15%, $S_m = 0.7$, and $S_f = -0.95$. Over an SNR range of 60–320, the SDs of the fit PSR, R_{1f}, and k_{mf} values were 0.4–2.2%, 0.01–0.03 s^{-1}, and 0.9–5.5 s^{-1}, respectively. This suggests that PSR and R_{1f} can be robustly determined from the in vivo brain data collected herein. Consistent with previous studies (Li et al., 2010), the uncertainty in k_{mf} is expected to be much larger, especially in lower SNR regions.

Following this fitting procedure, qMT parameter maps were smoothed with a locally-adaptive Gaussian filter (kernel size = $10 \times 10 \times 9$ mm^3, full width at half maximum = 1/2 kernel size) to remove outliers that tended to occur at tissue boundaries. To perform this operation, each filtered map was subtracted from the raw parameter map, and outliers were defined as voxels whose value was three standard deviations above the mean difference across all voxels. For these outliers, the value in the raw parameter map was replaced with the value in the filtered map. This process was iterated until the number of outliers was less than the expected value (0.3% of the total number of voxels).

Statistics

Mean qMT parameters (PSR, R_{1f}, and k_{mf}) were calculated within the following regions-of-interest (ROI): head of the caudate, putamen, thalamus, genu and splenium of the corpus callosum, internal capsule, corona radiata, occipital WM, and frontal WM. Statistical comparisons were performed on the mean ROI values to evaluate each parameter's i) variation across ROIs (i.e., regional differences), ii) variation and reproducibility across time, and iii) variation across volunteers. To compare parameters across WM regions, a non-parametric Wilcoxon rank-sum test was performed, with a $p < 0.05$ deeming a significant difference between ROI values. To evaluate the test–retest reproducibility of each parameter, a Bland–Altman (BA) analysis was performed. For the BA analysis, the mean difference and the limits of agreement (LOA = mean difference ± 1.96 * SD) were tabulated across scans for all ROIs. Additionally, a Wilcoxon signed-rank test was performed between the test and retest parameter values for each ROI, with a $p > 0.05$ indicating a non-significant difference between scans at each time point. To assess the test–retest variability of each parameter within each ROI, the coefficient of variation was calculated from: $CV = \frac{S}{M}\left(\frac{2}{\sqrt{2}}\right) \times 100$, where S is the SD of the test–retest difference across subjects, M is the mean value across all test–retest scans and subjects, and the $\sqrt{2}$ term accounts for the propagation of uncertainty from the difference operation. The across-cohort variability of each parameter within each ROI was also assessed via: $CV_{cohort} = S/M * 100$, where S is the SD across the cohort and M is mean value across the cohort. All values are reported as the mean ± SD unless otherwise stated.

Results

The results of the numerical simulations designed to assess the effect of TFE readout on qMT parameter maps are shown in Fig. 3. In Fig. 3a, the evolution of M_{zf} during the TFE readout is shown for WM as a function of t_i. Note that this evolution is related to the k-space filter of the readout. It can be seen that the shape (width and rate of decay) of the k-space filter changes as a function of t_i, which manifests as a change in object blurring as a function of t_i. The effect of this on the qMT parameter maps is shown in Figs. 3b–d. It can be seen that the resulting qMT parameter maps are smoothed in the phase-encoding direction with little bias in the fit parameters. It should be noted, however, that PSR values were slightly underestimated in the WM region of the 1D test object. Additional simulations indicated that this bias increased as the size of the WM region decreased.

Fig. 4 displays PSR maps acquired with and without application of the post-TFE saturation train (see the SAT region in Fig. 1) as a function of t_d. For scans with the saturation train, the fit PSR values at

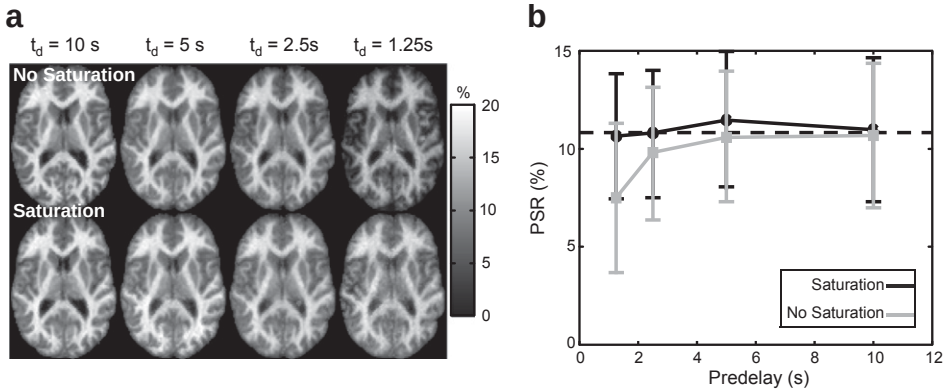

Fig. 4. (a) Maps of PSR as a function of t_d without (top) and with (bottom) a post-TFE saturation train and (b) corresponding mean (± SD) slice-wise PSR values. For scans with the saturation train, all PSR values were nearly identical to the values at full recovery (dashed line). Without the saturation train, PSR values were increasingly underestimated with decreasing t_d.

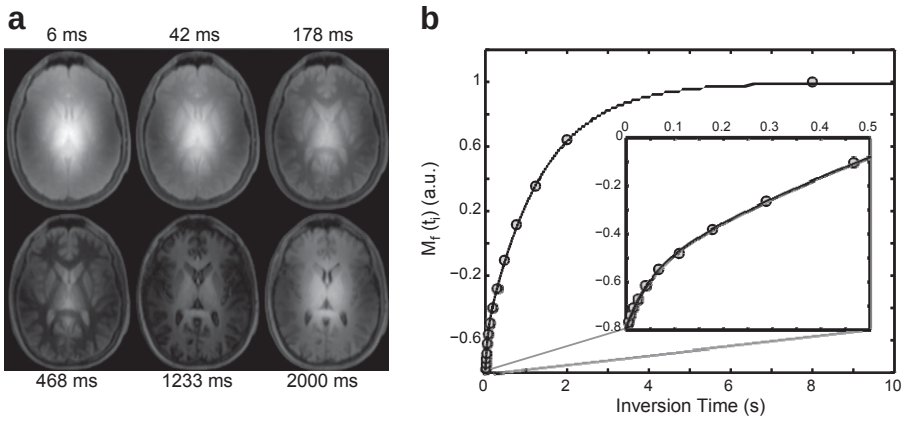

Fig. 5. Sample SIR-TFE images (a) and model fit (b) from a slice at the level of the lateral ventricles in a healthy control. (a) Images from six of the 14 inversion times are shown. Note the characteristic center brightening of the images due to B_1^+ inhomogeneities. (b) Corresponding SIR data from a voxel in the genu of the corpus callosum. Note the agreement between the SIR data (circles) and biexponential model [solid black line, Eq. (7)] and the deviation from a monoexponential model, which is apparent at the shortest inversion times shown in the zoomed inset.

shorter t_d values were nearly identical to those at full recovery (t_d = 10 s). Without this train, small deviations in PSR were observed at t_d = 2.5 s; and these were more pronounced at t_d = 1.25 s. Thus, the post-TFE saturation train allows for reduction of t_d (and scan times) with minimal parameter bias.

Representative 3D SIR-TFE data are shown in Fig. 5. Fig. 5a shows a single slice at the level of the lateral ventricles acquired at six of 14 t_i values. Note the characteristic center brightening due to B_1^+ inhomogeneities. Fig. 5b shows data from a single voxel in the genu of the corpus callosum and the corresponding model fit. Note the agreement between the SIR-TFE data and the biexponential model described by Eq. (7). Additionally, note the deviation from monoexponential recovery, which is especially evident at the shortest inversion times.

Based upon these fits, maps of qMT parameters were generated. Recall that these maps were filtered to reduce the impact of outliers. Fig. 6 displays representative qMT parameter maps without filtering, with the previously described locally-adaptive Gaussian filter, and with a global Gaussian filter. The locally-adaptive and global filters both removed outliers in the parameter maps (see arrow in the top row and the masks in the bottom row); however, the locally filtered maps were blurred to a much smaller degree. As a result, we employed the locally-adaptive approach herein. For all parameter maps, 14% of all voxels in the post-brain-extraction volume were smoothed using this approach. However, as seen in the bottom row of Fig. 6, a majority of these voxels were located along the brain surface or within the CSF.

Fig. 7 displays results from four representative slices in one healthy subject. The qMT parameters were uniform over most of the volume despite the presence of large !1B_0 and/or B_1^+ field inhomogeneities (as indicated by the heterogeneity in the S_m maps). There does, however, appear to be some bias in the qMT parameter values in midbrain slices (black arrow), which typically (Moore et al., 2010) exhibit the largest field inhomogeneities and the lowest SNR. Nevertheless, these data suggest that robust qMT parameter mapping can be achieved throughout most of the brain using the 3D SIR-TFE protocol described herein.

ROIs were defined in a number of WM and GM regions as shown in Fig. 8. The boxplots in the top row of Fig. 9 display the mean ROI qMT parameters over the 12 healthy volunteers. For PSR, the mean value across all WM ROIs (17.6 ± 1.3%) was higher than the values across all GM ROIs (10.3 ± 1.6%). Additionally, heterogeneity within WM PSR values was observed, but should be interpreted with caution due to the effect of multiple comparisons. Nevertheless, differences between the following regions were detected: i) the genu of the corpus callosum and occipital WM (p = 0.026), ii) the genu of the corpus callosum and the corona radiata (p = 0.026), iii) frontal and occipital WM (p = 0.041), and iv) frontal WM and the corona radiata (p = 0.041). Fit k_{mf} values were higher in GM (24.4 ± 4.4 s^{-1}) than in WM (14.5 ± 1.5 s^{-1}). Additionally, note the large, biased k_{mf} values in and

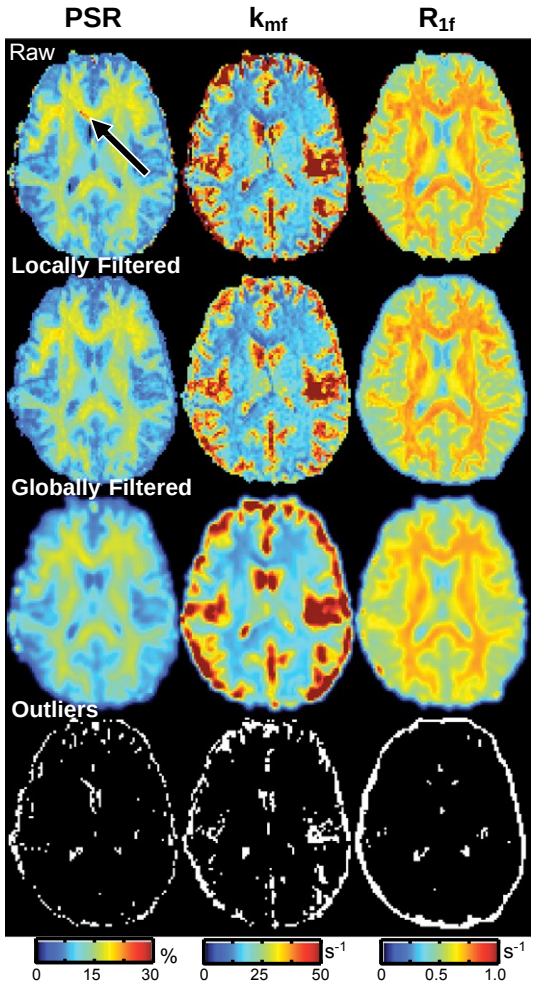

Fig. 6. Representative qMT parameter (PSR, k_{mf}, R_{1f}) maps with and without filtering. Shown are (1st row) raw parameter maps, (2nd row) parameter maps filtered with the locally-adaptive Gaussian filter, (3rd row) parameter maps filtered with the global Gaussian filter (with an identical kernel), and (4th row) masks of the outliers detected using the locally-adaptive filter. The arrow identifies a region with biased PSR values that are corrected by filtering. Note that the color-scale in these maps was chosen to highlight the outliers and is different than in Figs. 4 and 8.

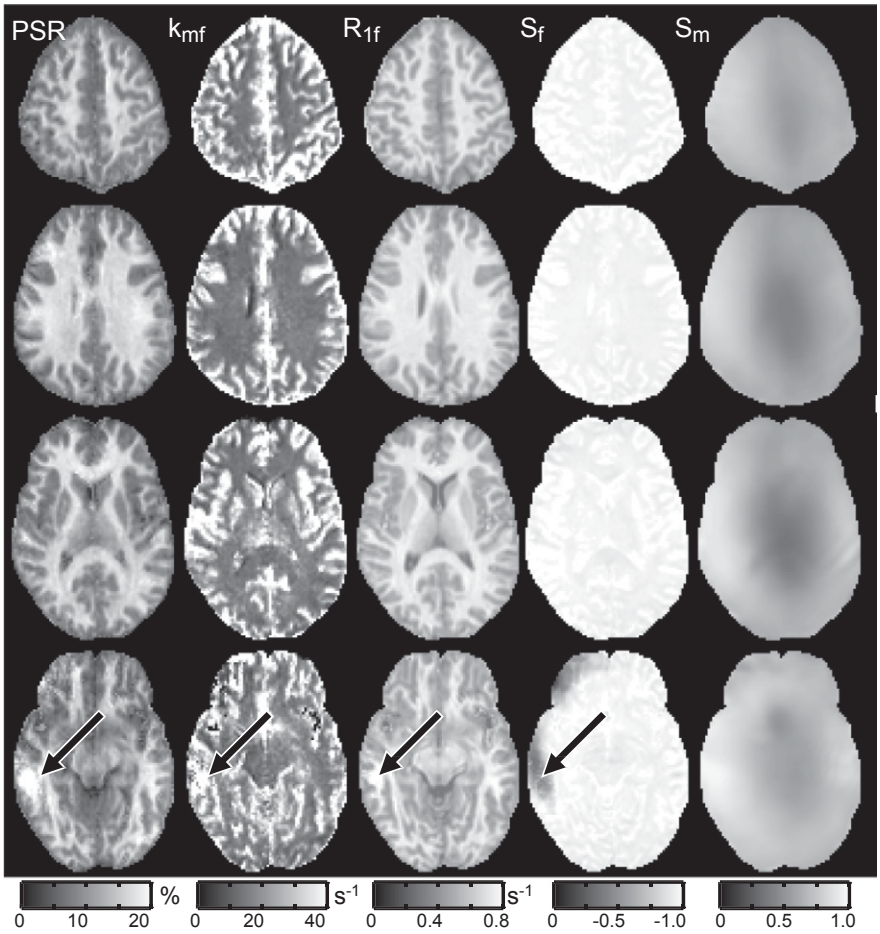

Fig. 7. Representative parameter maps from one subject (four of 30 slices are shown). The qMT parameters (PSR, k_{mf}, R_{1f}) and the inversion efficiency S_f were uniform over most of the volume despite the presence of large field inhomogeneities. There does, however, appear to be some bias in the qMT parameter values in midbrain slices (black arrows), which typically exhibit the largest B_0 and B_1^+ inhomogeneities. This results in a deviation of S_f from − 1 in these regions.

around areas containing CSF, which is likely a consequence of the weak dependence of the signal on k_{mf} when PSR ≈ 0 (see the simulated data in Fig. 3c). For R_{1f}, differences between WM ($0.73 \pm 0.03\ s^{-1}$) and GM ($0.58 \pm 0.05\ s^{-1}$) values were also observed. The boxplots in Fig. 9 give an indication of the variability of each parameter across the healthy cohort. To quantify this, the coefficient of variation was tabulated for each ROI, and the mean value across all ROI is given in Table 1. From this, it can be seen that the mean CV_{cohort} was b 10% for all of the qMT parameters, which is not surprising given the small age range of the healthy cohort scanned herein.

BA plots of the observed difference in mean ROI qMT parameters between scans are shown in the bottom row of Fig. 9; and the results from this analysis are given numerically in Table 1. The mean difference for all ROIs across scans was close to zero for PSR (0.0%), k_{mf} ($1.2\ s^{-1}$), and R_{1f} ($0.01\ s^{-1}$), indicating a lack of bias and reasonable reproducibility. To further test this, a Wilcoxon signed-rank test was performed on the test–retest parameter values in each ROI. At the $p = 0.05$ level, no significant difference was observed between test and retest qMT parameters in any of the ROIs except for k_{mf} in the genu of the corpus callosum ($p = 0.031$). The test–retest coefficient of variation (CV_{retest}) was also tabulated for each metric to further assess each parameter's variability across time. As shown in Table 1, the relative CV_{retest} values were consistent with the corresponding CV_{cohort} values, with k_{mf} exhibiting the highest variability. In terms of absolute CV values, the test–retest variability was approximately 20% lower than the across cohort variability.

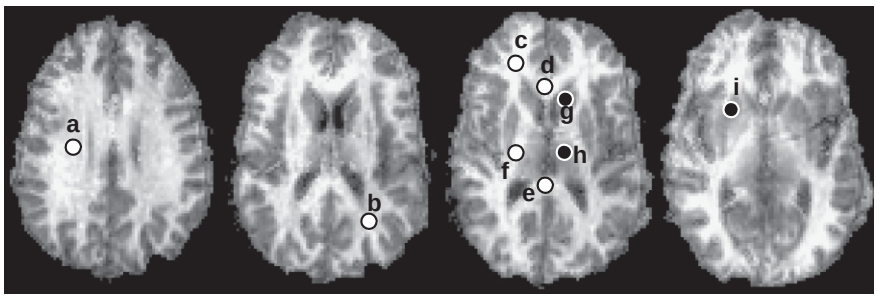

Fig. 8. Representative PSR maps from a single volunteer with corresponding ROIs (a = corona radiata; b = occipital WM; c = frontal WM; d = corpus callosum, genu; e = corpus callosum, splenium; f = internal capsule; g = head of caudate; h = thalamus; i = putamen). White and black dots represent WM and GM ROIs, respectively. In practice, ROIs were defined bilaterally and results were averaged across hemispheres. Here we show ROIs in one hemisphere for display purposes.

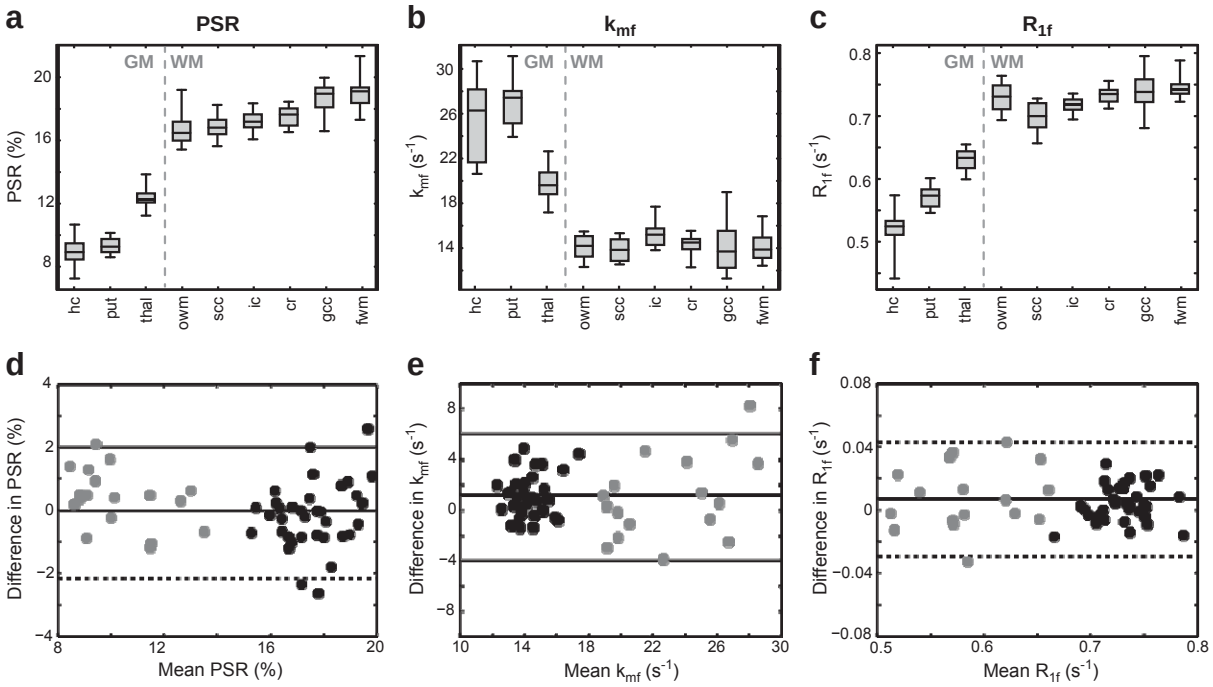

Fig. 9. (a–c) Boxplot of the mean ROI qMT parameters (hc = head of caudate; put = putamen; thal = thalamus; owm = occipital WM; scc = corpus callosum, splenium; ic = internal capsule; cr = corona radiata; gcc = corpus callosum, genu; fwm = frontal WM). On each box, the central mark is the median, the edges of the box are the 25th and 75th percentiles, and the whiskers extend to the most extreme data points. (d–f) Bland–Altman plots of the difference in parameters for WM (black) and GM (gray) ROIs across scans. The solid line is the mean difference, and the dashed lines are the limits of agreement (mean difference ± 1.96 SD).

Discussion

This study demonstrates the feasibility of performing whole-brain qMT measurements in the human brain in vivo at high field. Pulsed saturation and SSFP-based approaches are difficult to implement at high field due to RF power limitations and/or magnetic field (B_1^+ and $!1B_0$) inhomogeneities. In this study, we employed the SIR qMT approach, which has been suggested to be less sensitive to these issues. The biggest obstacles to overcome were i) the effect of B_1^+ and $!1B_0$ inhomogeneities on the inversion pulse and the readout and ii) the long scan times associated with SIR imaging. The former of these was mitigated by developing a novel B_1^+ and $!1B$ insensitive inversion composite pulse (Fig. 2) and employing a low-flip angle TFE readout; the latter was mitigated by the efficiency of the TFE readout along with additional protocol optimization (e.g., reducing the number of t_i values to 14, applying SENSE acceleration in two directions). Together this resulted in a robust (Fig. 9), whole-brain qMT imaging protocol with a scan time of less than 20 min.

Previous qMT imaging studies at lower field strengths (Dortch et al., 2011; Garcia et al., 2010; Gloor et al., 2008; Ropele et al., 2003; Sled and Pike, 2001; Sled et al., 2004; Yarnykh and Yuan, 2004) have reported PSR values in the range of 11–16% and 5–9% for WM and GM structures, respectively [PSR = F using the notation of Sled and Pike (2000, 2001) and M_{0b} using the notation of Henkelman et al. (1993)]. The PSR values presented herein (WM: 15–20%, GM: 9–13%) were approximately 25% higher. PSR should be independent of field strength, so these differences may be related to the SIR-TFE sequence. As previously discussed, we modified the inversion pulse and readout of our 3.0-T SIR-FSE sequence to perform qMT imaging at 7.0 T. The effect of the TFE readout on the fit qMT parameters was assessed via numerical simulations and was found to result in little bias in PSR (Fig. 3). However, it should be noted that our previous report at 3.0 T employed a much longer TE (74 ms) than was employed herein (1.4 ms). Previous work (Bjarnason et al., 2005; Stanisz et al., 1999) has demonstrated that MT contrast is TE-dependent in WM due to the microanatomical compartition of water into myelin and nonmyelin water spaces. As a result, it is reasonable to assume that PSR may also exhibit a TE-dependence. In terms of the inversion pulse, we recognize that PSR is sensitive to the macromolecular pool lineshape and T_{2m} assumptions used in the numerical estimation of S_m. Similar to our previous studies (Dortch et al., 2011; Gochberg and Gore, 2007), we modeled the macromolecular pool using a Gaussian lineshape (T_{2m} = 10 !s) because the Super-Lorentzian exhibits an on-resonance singularity. Previous work using a 1-ms block inversion pulse at 3.0 T (Dortch et al., 2011) found that this was a reasonable approximation; however, this may not be true for the longer (5.5 ms), higher power composite inversion pulse employed herein. Additional work is needed to explore the field- and TE-dependence of PSR values obtained via the SIR technique. Nevertheless, the reported regional variation in PSR values was consistent with previous qMT imaging studies (Dortch et al., 2011;

Table 1
Test–retest reproducibility analysis of each qMT parameter (PSR, R_{1f}, and k_{mf}). Shown are the mean ± SD parameter values across all ROIs for the test and retest scans, the resulting mean paired-difference between time-points, the limits-of-agreement (LOA), and the mean ± SD test–retest coefficient of variation (CV_{retest}) across all ROIs. For comparison, the corresponding across-cohort coefficient of variation (CV_{cohort}) is also given.

Parameter	Test scan (mean ± SD)	Retest scan (mean ± SD)	Difference	LOA	CV_{retest} (%)	CV_{cohort} (%)
PSR (%)	15.2 ± 3.9	15.2 ± 3.7	0.0	(− 2.2, 2.1)	4.9 ± 1.5	5.6 ± 1.9
k_{mf} (s^{-1})	16.8 ± 4.7	18.0 ± 5.5	1.2	(− 3.9, 6.3)	8.2 ± 2.4	9.4 ± 3.6
R_{1f} (s^{-1})	0.68 ± 0.08	0.68 ± 0.08	0.01	(− 0.03, 0.04)	1.9 ± 1.4	3.2 ± 1.3

Garcia et al., 2010; Sled et al., 2004; Underhill et al., 2009); and additional SIR-TFE studies in bovine serum albumin phantoms at 7.0 T (data not shown) found a linear relationship between macromolecular content and PSR. Thus, we postulate that the regional differences in PSR values reported herein are driven primarily by regional differences in myelin content, although the absolute values may be systematically larger than reported by other techniques.

Previous pulsed saturation and SSFP-based studies (Garcia et al., 2010; Gloor et al., 2008; Ropele et al., 2003; Sled and Pike, 2001; Sled et al., 2004; Yarnykh and Yuan, 2004) report k_{mf} values [$k_{mf} = k_f / F$ using the notation of Sled and Pike (2000, 2001); $k_{mf} = R$ when $M_{0f} = 1$ using the notation of Henkelman et al. (1993)] in the range of 20–40 s^{-1} across the brain. A previous SIR study (Dortch et al., 2011) at 3.0 T reports k_{mf} values that are approximately 2-fold slower (10–15 s^{-1}) with values that are slower in WM than GM, which is consistent with the results presented herein. The discrepancies between techniques are not surprising given the reported difficulty of using pulsed saturation to determine k_{mf} (Portnoy and Stanisz, 2007). In terms of the current study, it should be noted that k_{mf} showed the largest variability of the qMT parameters, which is consistent with the results from the Monte Carlo simulations. We do not expect this to be a significant drawback as k_{mf} has been shown to be insensitive to the pathological changes in spinal cord WM (Smith et al., 2009).

While there have been no previous reports of R_{1f} in human brain at 7.0 T, it can be shown that the observed T_1 typically reported is $\approx 1/R_{1f}$. Using this relationship, the mean WM and GM observed T_1 values were 1372 and 1724 ms, respectively, which are within the range of previously reported values in human brain at 7.0 T (Wright et al., 2008). As expected, we noted a significant correlation between R_{1f} and PSR in the healthy human brain (data not shown); however, T_1 is sensitive to overall tissue composition [e.g., water content (Kiricuta and Simplaceanu, 1975)] and is believed to be a less specific marker for myelin in WM.

The increased SNR available at 7.0 T was used here to decrease scan time ($\approx$ 40 s/slice) and increase resolution ($2 \times 2 \times 3$ mm^3) relative to our 3.0-T protocol. Moving forward, it may be advantageous to look at higher resolution protocols. If we assume that all imaging parameters are the same, increasing the resolution to $1 \times 1 \times 3$ mm^3 would result in an approximately two-fold decrease in SNR ($\approx$ 70 at thermal equilibrium, assuming we increase the number of acquired points to hold the field-of-view constant). Based upon previous simulation work (Li et al., 2010) as well as the simulation work presented herein, this would be sufficient to robustly fit qMT parameters over most of the brain. Thus, it appears that high-resolution qMT imaging may be feasible in the human brain in vivo at 7.0 T using a protocol similar to that described herein.

Conclusions

The results of this study demonstrate the feasibility of performing qMT imaging in human brain in vivo at high field. The developed SIR-TFE protocol allowed for whole-brain qMT imaging in less than 20 min. In healthy subjects, intra-subject reliability (i.e., test–retest) was demonstrated despite large ΔB_0 and B_1^+ variations. Additionally, a high level of inter-subject reproducibility was demonstrated for the qMT parameters. Future work includes investigating high-resolution protocols to look at cortical features of qMT parameters and application of the approach in a cohort of multiple sclerosis patients.

Acknowledgments

This work was supported by NIH/NBIB K01 EB009120 (SAS), NIH T32 EB001628 (JCG), NIH EB00461 (JCG), and Vanderbilt Bridge Funding (DFG).

References

Berry, I., Barker, G., Barkhof, F., Campi, A., Dousset, V., Franconi, J., Gass, A., Schreiber, W., Miller, D., Tofts, P., 1999. A multicenter measurement of magnetization transfer ratio in normal white matter. J. Magn. Reson. Imaging 9, 441–446.

Bjarnason, T., Vavasour, I., Chia, C., Mackay, A., 2005. Characterization of the NMR behavior of white matter in bovine brain. Magn. Reson. Med. 54, 1072–1081.

Bruno, S.D., Barker, G.J., Cercignani, M., Symms, M., Ron, M.A., 2004. A study of bipolar disorder using magnetization transfer imaging and voxel-based morphometry. Brain 127, 2433–2440.

Catalaa, I., Grossman, R.I., Kolson, D.L., Udupa, J.K., Nyul, L.G., Wei, L., Zhang, X., Polansky, M., Mannon, L.J., McGowan, J.C., 2000. Multiple sclerosis: magnetization transfer histogram analysis of segmented normal-appearing white matter. Radiology 216, 351–355.

Cercignani, M., Alexander, D., 2006. Optimal acquisition schemes for in vivo quantitative magnetization transfer MRI. Magn. Reson. Med. 56, 803–810.

Constable, R.T., Gore, J.C., 1992. The loss of small objects in variable TE imaging: implications for FSE, RARE, and EPI. Magn. Reson. Med. 28, 9–24.

Dortch, R.D., Li, K., Gochberg, D.F., Welch, E.B., Dula, A.N., Tamhane, A.A., Gore, J.C., Smith, S.A., 2011. Quantitative magnetization transfer imaging in human brain at 3 T via selective inversion recovery. Magn. Reson. Med. 66, 1346–1352.

Dousset, V., Grossman, R.I., Ramer, K.N., Schnall, M.D., Young, L.H., Gonzalez-Scarano, F., Lavi, E., Cohen, J.A., 1992. Experimental allergic encephalomyelitis and multiple sclerosis: lesion characterization with magnetization transfer imaging. Radiology 182, 483–491.

Edzes, H.T., Samulski, E.T., 1977. Cross relaxation and spin diffusion in the proton NMR or hydrated collagen. Nature 265, 521–523.

Filippi, M., Rocca, M.A., 2004. Magnetization transfer magnetic resonance imaging in the assessment of neurological diseases. J. Neuroimaging 14, 303–313.

Garcia, M., Gloor, M., Wetzel, S.G., Radue, E.-W., Scheffler, K., Bieri, O., 2010. Characterization of normal appearing brain structures using high-resolution quantitative magnetization transfer steady-state free precession imaging. NeuroImage 52, 532–537.

Gass, A., Barker, G.J., Kidd, D., Thorpe, J.W., MacManus, D., Brennan, A., Tofts, P.S., Thompson, A.J., McDonald, W.I., Miller, D.H., 1994. Correlation of magnetization transfer ratio with clinical disability in multiple sclerosis. Ann. Neurol. 36, 62–67.

Gloor, M., Scheffler, K., Bieri, O., 2008. Quantitative magnetization transfer imaging using balanced SSFP. Magn. Reson. Med. 60, 691–700.

Gochberg, D., Gore, J., 2007. Quantitative magnetization transfer imaging via selective inversion recovery with short repetition times. Magn. Reson. Med. 57, 437–441.

Gochberg, D., Kennan, R., Gore, J., 1997. Quantitative studies of magnetization transfer by selective excitation and T_1 recovery. Magn. Reson. Med. 38, 224–231.

Graham, S.J., Henkelman, R.M., 1997. Understanding pulsed magnetization transfer. J. Magn. Reson. Imaging 7, 903–912.

Henkelman, R., Huang, X., Xiang, Q., Stanisz, G., Swanson, S., Bronskill, M., 1993. Quantitative interpretation of magnetization transfer. Magn. Reson. Med. 29, 759–766.

Kabani, N.J., Sled, J.G., Chertkow, H., 2002a. Magnetization transfer ratio in mild cognitive impairment and dementia of Alzheimer's type. NeuroImage 15, 604–610. Kabani, N.J., Sled, J.G., Shuper, A., Chertkow, H., 2002b. Regional magnetization transfer ratio changes in mild cognitive impairment. Magn. Reson. Med. 47, 143–148.

Kalkers, N.F., Hintzen, R.Q., van Waesberghe, J.H., Lazeron, R.H., van Schijndel, R.A., Ader, H.J., Polman, C.H., Barkhof, F., 2001. Magnetization transfer histogram parameters reflect all dimensions of MS pathology, including atrophy. J. Neurol. Sci. 184, 155–162.

Kiricuta Jr., I.C., Simplaceanu, V., 1975. Tissue water content and nuclear magnetic resonance in normal and tumor tissues. Cancer Res. 35, 1164–1167.

Koenig, S.H., 1991. Cholesterol of myelin is the determinant of gray–white contrast in MRI of brain. Magn. Reson. Med. 20, 285–291.

Kucharczyk, W., Macdonal, P., Stanisz, G., Henkelman, R., 1994. Relaxivity and magnetization transfer of white matter lipids at MR imaging: importance of cerebrosides and pH. Radiology 192, 521–529.

Levesque, I.R., Sled, J.G., Pike, G.B., 2011. Iterative optimization method for design of quantitative magnetization transfer imaging experiments. Magn. Reson. Med. 66, 635–643.

Li, K., Zu, Z., Xu, J., Janve, V.A., Gore, J.C., Does, M.D., Gochberg, D.F., 2010. Optimized inversion recovery sequences for quantitative T_1 and magnetization transfer imaging. Magn. Reson. Med. 64, 491–500.

Moore, J., Jankiewicz, M., Zeng, H., Anderson, A.W., Gore, J.C., 2010. Composite RF pulses for B_1^+-insensitive volume excitation at 7 Tesla. J. Magn. Reson. 205, 50–62.

Morrison, C., Stanisz, G., Henkelman, R.M., 1995. Modeling magnetization transfer for biological-like systems using a semi-solid pool with a super-Lorentzian lineshape and dipolar reservoir. J. Magn. Reson. B 108, 103–113.

Mougin, O.E., Coxon, R.C., Pitiot, A., Gowland, P.A., 2010. Magnetization transfer phenomenon in the human brain at 7 T. NeuroImage 49, 272–281.

Mugler III, J.P., Brookeman, J.R., 1990. Three-dimensional magnetization-prepared rapid gradient-echo imaging (3D MP RAGE). Magn. Reson. Med. 15, 152–157.

Odrobina, E., Lam, T., Pun, T., Midha, R., Stanisz, G., 2005. MR properties of excised neural tissue following experimentally induced demyelination. NMR Biomed. 18, 277–284.

Ou, X., Sun, S.W., Liang, H.F., Song, S.K., Gochberg, D.F., 2009. The MT pool size ratio and the DTI radial diffusivity may reflect the myelination in shiverer and control mice. NMR Biomed. 22, 480–487.

Pike, G.B., 1996. Pulsed magnetization transfer contrast in gradient echo imaging: a two-pool analytic description of signal response. Magn. Reson. Med. 36, 95–103.

Portnoy, S., Stanisz, G.J., 2007. Modeling pulsed magnetization transfer. Magn. Reson. Med. 58, 144–155.

Ramani, A., Dalton, C., Miller, D.H., Tofts, P.S., Barker, G.J., 2002. Precise estimate of fundamental in-vivo MT parameters in human brain in clinically feasible times. Magn. Reson. Imaging 20, 721–731.

Ropele, S., Seifert, T., Enzinger, C., Fazekas, F., 2003. Method for quantitative imaging of the macromolecular ^{1}H fraction in tissues. Magn. Reson. Med. 49, 864–871.

Schmierer, K., Scaravilli, F., Altmann, D., Barker, G., Miller, D., 2004. Magnetization transfer ratio and myelin in postmortem multiple sclerosis brain. Ann. Neurol. 56, 407–415.

Schmierer, K., Tozer, D.J., Scaravilli, F., Altmann, D.R., Barker, G.J., Tofts, P.S., Miller, D.H., 2007. Quantitative magnetization transfer imaging in postmortem multiple sclerosis brain. J. Magn. Reson. Imaging 26, 41–51.

Sled, J.G., Pike, G.B., 2000. Quantitative interpretation of magnetization transfer in spoiled gradient echo MRI sequences. J. Magn. Reson. 145, 24–36.

Sled, J.G., Pike, G.B., 2001. Quantitative imaging of magnetization transfer exchange and relaxation properties in vivo using MRI. Magn. Reson. Med. 46, 923–931.

Sled, J.G., Levesque, I., Santos, A.C., Francis, S.J., Narayanan, S., Brass, S.D., Arnold, D.L., Pike, G.B., 2004. Regional variations in normal brain shown by quantitative magnetization transfer imaging. Magn. Reson. Med. 51, 299–303.

Smith, S.M., 2002. Fast robust automated brain extraction. Hum. Brain Mapp. 17, 143–155.

Smith, S., Golay, X., Fatemi, A., Mahmood, A., Raymond, G., Moser, H., van Zijl, P., Stanisz, G., 2009. Quantitative magnetization transfer characteristics of the human cervical spinal cord in vivo: application to adrenomyeloneuropathy. Magn. Reson. Med. 61, 22–27.

Stanisz, G., Kecojevic, A., Bronskill, M., Henkelman, R., 1999. Characterizing white matter with magnetization transfer and T_2. Magn. Reson. Med. 42, 1128–1136.

Underhill, H.R., Yuan, C., Yarnykh, V.L., 2009. Direct quantitative comparison between cross-relaxation imaging and diffusion tensor imaging of the human brain at 3.0 T. NeuroImage 47, 1568–1578.

Underhill, H.R., Rostomily, R.C., Mikheev, A.M., Yuan, C., Yarnykh, V.L., 2011. Fast bound pool fraction imaging of the in vivo rat brain: association with myelin content and validation in the C6 glioma model. NeuroImage 54, 2052–2065.

Viola, P., Wells, W.M., 1997. Alignment by maximization of mutual information. Int. J. Comput. Vis. 24, 137–154.

Wolff, S.D., Balaban, R.S., 1989. Magnetization transfer contrast (MTC) and tissue water proton relaxation in vivo. Magn. Reson. Med. 10, 135–144.

Wright, P.J., Mougin, O.E., Totman, J.J., Peters, A.M., Brookes, M.J., Coxon, R., Morris, P.E., Clemence, M., Francis, S.T., Bowtell, R.W., Gowland, P.A., 2008. Water proton T_1 measurements in brain tissue at 7, 3, and 1.5 T using IR-EPI, IR-TSE, and MPRAGE: results and optimization. MAGMA 21, 121–130.

Yarnykh, V.L., 2007. Actual flip-angle imaging in the pulsed steady state: a method for rapid three-dimensional mapping of the transmitted radiofrequency field. Magn. Reson. Med. 57, 192–200.

Yarnykh, V.L., Yuan, C., 2004. Cross-relaxation imaging reveals detailed anatomy of white matter fiber tracts in the human brain. NeuroImage 23, 409–424.